Icarus 254 (2015) 287–305

Contents lists available at ScienceDirect

Icarus

journal homepage: www.elsevier.com/locate/icarus

Orbital multispectral mapping of Mercury with the MESSENGER Mercury Dual Imaging System: Evidence for the origins of plains units and low-reflectance material

Scott L. Murchie[a,*], Rachel L. Klima[a], Brett W. Denevi[a], Carolyn M. Ernst[a], Mary R. Keller[a], Deborah L. Domingue[b], David T. Blewett[a], Nancy L. Chabot[a], Christopher D. Hash[c], Erick Malaret[c], Noam R. Izenberg[a], Faith Vilas[b], Larry R. Nittler[d], Jeffrey J. Gillis-Davis[e], James W. Head[f], Sean C. Solomon[d,g]

[a] The Johns Hopkins University Applied Physics Laboratory, Laurel, MD 20723, USA
[b] Planetary Science Institute, Tucson, AZ 85719, USA
[c] Applied Coherent Technology Corporation, Herndon, VA 20170, USA
[d] Department of Terrestrial Magnetism, Carnegie Institution of Washington, Washington, DC 20015, USA
[e] Hawaii Institute of Geophysics and Planetology, University of Hawaii, Honolulu, HI, 96822, USA
[f] Department of Earth, Environmental and Planetary Sciences, Brown University, Providence, RI 02912, USA
[g] Lamont-Doherty Earth Observatory, Columbia University, Palisades, NY 10964, USA

ARTICLE INFO

Article history:
Received 27 August 2014
Revised 23 March 2015
Accepted 25 March 2015
Available online 31 March 2015

Keywords:
Mercury, surface
Volcanism
Spectroscopy
Mineralogy

ABSTRACT

A principal data product from MESSENGER's primary orbital mission at Mercury is a global multispectral map in eight visible to near-infrared colors, at an average pixel scale of 1 km, acquired by the Mercury Dual Imaging System. The constituent images have been calibrated, photometrically corrected to a standard geometry, and map projected. Global analysis reveals no spectral units not seen during MESSENGER's Mercury flybys and supports previous conclusions that most spectral variation is related to changes in spectral slope and reflectance between spectral end-member high-reflectance red plains (HRP) and low-reflectance material (LRM). Comparison of color properties of plains units mapped on the basis of morphology shows that the two largest unambiguously volcanic smooth plains deposits (the interior plains of Caloris and the northern plains) are close to HRP end members and have average color properties distinct from those of most other smooth plains and intercrater plains. In contrast, smaller deposits of smooth plains are nearly indistinguishable from intercrater plains on the basis of their range of color properties, consistent with the interpretation that intercrater plains are older equivalents of smooth plains. LRM having nearly the same reflectance is exposed in crater and basin ejecta of all ages, suggesting impact excavation from depth of material that is intrinsically dark or darkens very rapidly, rather than gradual darkening of exposed material purely by space weathering. A global search reveals no definitive absorptions attributable to Fe^{2+}-containing silicates or to sulfides over regions 20 km or more in horizontal extent, consistent with results from MESSENGER's Mercury Atmospheric and Surface Composition Spectrometer. The only absorption-like feature identified is broad upward curvature of the spectrum centered near 600 nm wavelength. The feature is strongest in freshly exposed LRM and weak or absent in older exposures of LRM. We modeled spectra of LRM as intimate mixtures of HRP with candidate low-reflectance phases having a similar 600-nm spectral feature, under the assumption that the grain size is 1 μm or larger. Sulfides measured to date in the laboratory and coarse-grained iron are both too bright to produce LRM from HRP. Ilmenite is sufficiently dark but would require Ti abundances too high to be consistent with MESSENGER X-Ray Spectrometer measurements. Three phases or mixtures of phases that could be responsible for the low reflectance of LRM are consistent with our analyses. Graphite, in amounts consistent with upper limits from the Gamma-Ray Spectrometer, may be consistent with geochemical models of Mercury's differentiation calling for a graphite-enriched primary flotation crust from an early magma ocean and impact mixing of that early crust before or during the late heavy bombardment (LHB) into material underlying the volcanic plains. The grain size of preexisting iron or iron sulfide could have been altered to a mix of nanophase and microphase grains

---

* Corresponding author at: The Johns Hopkins University Applied Physics Laboratory, 11101 Johns Hopkins Road, Laurel, MD 20723, USA.
E-mail address: scott.murchie@jhuapl.edu (S.L. Murchie).

http://dx.doi.org/10.1016/j.icarus.2015.03.027

by shock during those impacts, lowering reflectance. Alternatively, iron-bearing phases and carbon in a late-accreting carbonaceous veneer may have been stirred into the lower crust or upper mantle. Decoupling of variations in color from abundances of major elements probably results from the very low content and variation of Fe^{2+} in crustal silicates, such that reflectance is controlled instead by one or more minor opaque phases and the extent of space weathering.

1. Introduction and background

Multispectral imaging of airless rocky bodies at wavelengths of 0.4–1.0 μm provides important constraints on endogenic and exogenic surface processes. Key variables that affect spectral reflectance at these wavelengths include the amount and oxidation state of transition metals, principally iron, in silicates and oxides; the presence of opaque components, including ilmenite and carbon-bearing phases; and the degree of space weathering, the modification of the optical properties of the surface by sustained interaction with the space environment. Iron in minerals creates crystal-field absorptions near 0.85–1.05 μm that are particularly important in distinguishing key Fe-bearing phases, including oxides, olivine, and pyroxene, and in detecting variations in Fe content within pyroxene and olivine. Opaque minerals typically darken and flatten the reflectance spectrum of a mixture in which they occur. Space weathering occurs on the Moon and near-Earth asteroids and is inferred to occur on Mercury, by the deposition of sub-microscopic iron-rich rims on regolith grains from impact-generated vapor and solar wind sputtering (e.g., Hapke, 2001; Gaffey et al., 1993; Pieters, 1993; Hapke, 2001; Domingue et al., 2014). Space weathering on those bodies has the effect of darkening and reddening silicate spectra at these wavelengths. Both opaque minerals and space weathering also tend to subdue mineralogic absorptions.

In this paper, we describe the collection, processing, and first results from analysis of the global multispectral map of Mercury at 0.4–1.0 μm collected by the Mercury Dual Imaging System (MDIS) wide-angle camera (WAC) (Hawkins et al., 2007, 2009) on the MErcury Surface, Space ENvironment, GEochemistry, and Ranging (MESSENGER) spacecraft (Solomon et al., 2001). The map addresses three major science objectives (Solomon et al., 2001; Hawkins et al., 2007): (a) constraining formation of geologic units on the basis of discrete differences in color as stratigraphic markers; (b) constraining mineralogical composition and compositional heterogeneity of the surface on the basis of overall reflectance, spectral slope, and any absorption features; and (c) understanding surface processes, including space weathering, from reflectance and color trends. An overarching theme common to all three objectives is how the surface of Mercury compares with other airless silicate-rich planetary surfaces. Below we summarize the comparative planetologic context of that theme.

On the Moon, there are three primary causes for variations in color from near-ultraviolet to near-infrared wavelengths. First, the modal abundance of iron-rich pyroxene varies between the basaltic maria and anorthositic highlands, resulting in a lower reflectance and stronger 1-μm absorption in the maria (Pieters, 1993; Adams and McCord, 1970). Second, within the maria, variations in ultraviolet to visible reflectance and spectral slope are caused by differences in the abundance of the opaque mineral ilmenite ($FeTiO_3$). Both of these compositional variations can be measured, to first order, from color and average reflectance (Charette et al., 1974; Lucey et al., 1995, 1998; Blewett et al., 1997). The third source of variability is the length of time since material was exposed at the surface by impacts or mass wasting. "Optical maturation" (darkening and reddening) of regolith by space weathering (e.g., Hapke, 2001) is quantifiable as the change in reflectance and spectral slope from those of fresh material toward those of a theoretical, hyper-weathered end member (Lucey et al., 1995, 1998; Blewett et al., 1997).

Two moderate-sized to large asteroids have been globally imaged multispectrally by spacecraft, and they exhibit spectral variations distinct from each other and from those of the Moon. 433 Eros, at an average heliocentric distance of 1.45 AU, was imaged by the Multispectral Imager on the Near Earth Asteroid Rendezvous (NEAR) Shoemaker spacecraft. The Asteroid 4 Vesta, at an average heliocentric distance of 2.36 AU, was imaged by the Framing Camera on the Dawn spacecraft. On Eros, there is no evidence for distinct compositional units or for large regional differences in mineral abundances (Bell et al., 2002; Izenberg et al., 2003), consistent with the hypothesis that the asteroid is a primitive, undifferentiated object. Freshly exposed materials are darkened by space weathering but show less reddening and a smaller decrease in absorption depths than on the Moon (Clark et al., 2001; Murchie et al., 2002). Samples returned to Earth by the Hayabusa spacecraft from the compositionally analogous near-Earth Asteroid 25143 Itokawa have grain rims more dominated by sulfides than those on the Moon, pointing to chemical differences in how rims of regolith grains are modified as the reason for the different spectral effects of space weathering on the Moon and undifferentiated asteroids (Noguchi et al., 2011, 2014).

On Vesta, a differentiated asteroid (Russell et al., 2012), multispectral imaging has revealed evidence for variations in pyroxene composition from lower- to higher-Fe forms from inside to outside the large Rheasilvia south polar impact feature, and for a dark, spectrally neutral component for which the abundance varies regionally (De Sanctis et al., 2012; McCord et al., 2012; Pieters et al., 2012; Reddy et al., 2012a,b). The dark component has a much greater effect on overall reflectance than does variation in pyroxene composition. Correlation of reflectance with hydrogen abundance suggests that the dark component is exogenic carbonaceous chondrite- (CC)-like material, consistent with exotic CC clasts observed in howardite–eucrite–diogenite meteorites derived from Vesta (McCord et al., 2012; Prettyman et al., 2012; Reddy et al., 2012a,b). Space weathering on Vesta occurs without the reddening and weakening of absorptions observed on the Moon and instead is more equivalent to mixing of the spectral end members. This difference may be due to Vesta's greater heliocentric distance and hence lower impact velocities, leading to less impact heating, lesser rates of formation of grain coatings, and a dominance of comminution and mixing (Pieters et al., 2012).

Multispectral imaging by MDIS shows that Mercury is distinct spectrally from all three bodies discussed above. Three flybys in 2008–2009 provided nearly 98% coverage but only regional coverage at the low to moderate incidence and emergence angles preferred for spectral measurements. Since MESSENGER's orbit insertion on 18 March 2011, 99.8% coverage at higher spatial resolution has been acquired at near-nadir geometries, at close to the minimum incidence angles available as a function of latitude. Mercury's surface contains widespread, smooth volcanic plains (Robinson and Lucey, 1997; Head et al., 2008; Denevi et al., 2009). From early observations, one characteristic of smooth plains appeared to be a higher reflectance and steeper spectral slope, i.e., redder color (Robinson and Lucey, 1997; Murchie et al., 2008). Subsequent work showed that smooth plains vary in color from lower reflectance and a less red spectral slope, through higher reflectance and a redder slope. There is a continuous range of variation, with reflectance at 0.75 μm from $\sim$0.8 to 1.25 that of the average surface (Denevi et al., 2009).

Three major spectral units within smooth plains, a major unit corresponding to the darkest materials on the surface, and three minor spectral units are among those identified on Mercury from MDIS data (Table 1). Recognized plains units include low-reflectance blue plains (LBP), intermediate plains (IP), and high-reflectance red plains (HRP) (Denevi et al., 2009). Low-reflectance material (LRM) is darker and less red than LBP and is strongly concentrated on the floors and rims and in the ejecta of impact craters and basins. A broad, shallow absorption-like feature in LRM centered near 600 nm (described hereafter as the 600-nm feature) led to an initial interpretation that its darkening phase could be ilmenite or another Ti-bearing phase, as on the Moon (Robinson et al., 2008; Denevi et al., 2009). A more heavily cratered spectral unit having color and reflectance comparable to those of IP has been recognized and termed intermediate terrain (IT) (Denevi et al., 2009). In Section 4.2 we show that there are also more heavily cratered equivalents of both HRP and LBP.

The three minor spectral units, all comparatively high in reflectance, are distinctive. First, fresh crater materials are brighter at all wavelengths and less red than plains or LRM, consistent with less space weathering (Robinson et al., 2008; Blewett et al., 2009). However, immature materials are 30–50% lower in reflectance than immature materials in the lunar highlands, suggesting that an indigenous darkening component is present in most or all crustal materials, not just LRM (Robinson et al., 2008; Denevi and Robinson, 2008; Braden and Robinson, 2013). Second, a "red unit" consisting of pyroclastic deposits (Robinson et al., 2008; Goudge et al., 2014) is brighter and redder than HRP. Third, bright hollows materials within and in haloes around hollows' depressions (Blewett et al., 2011) are comparable in reflectance to plains at the longest wavelengths covered by MDIS, but are less red and brighter at shorter wavelengths. Hollows are closely associated with LRM (Robinson et al., 2008; Blewett et al., 2011, 2013). None of these units exhibits an identifiable 1-μm crystal field absorption due to ferrous iron in silicates, consistent with ground-based observations that indicate a very weak or nonexistent 1-μm absorption, and an Fe^{2+} content in surface silicates of <3 wt% (McCord and Clark, 1979; Vilas, 1988; Warell and Blewett, 2004).

Elemental abundance measurements obtained since MESSENGER began orbital operations further constrain mechanisms responsible for color variations. X-Ray Spectrometer (XRS) and Gamma-Ray Spectrometer (GRS) data confirm a low total Fe abundance with a global range of $\sim$1–2 wt% (1.3–2.6 wt% FeO) (Nittler et al., 2011; Weider et al., 2012, 2014) and an average abundance over the northern hemisphere of 1.9 ± 0.3 wt% (Evans et al., 2012). Average Ti abundance is $\leqslant$0.8 wt% ($\leqslant$1.3 wt% TiO_2) (Nittler et al., 2011). Sulfur is unexpectedly abundant, with a global range of $\sim$1–4 wt% S (Nittler et al., 2011; Weider et al., 2012) and a northern hemisphere average of 2.3 ± 0.4 wt% S (Evans et al., 2012). The measured Fe abundance, though low, would still be expected to result in a 1-μm absorption several percent or more in depth if the Fe were in silicates (Klima et al., 2011). Modeling indicates that the low abundance of Fe and high abundance of S are consistent with a highly reducing environment, for which sulfide–silicate melt equilibria predict that Fe will be present in sulfide or metal instead of in silicates (Zolotov et al., 2013). The high S and low Ti abundances have also led to suggestions that a sulfide, instead of ilmenite, could be the darkening agent in LRM (Blewett et al., 2013; Helbert et al., 2013).

In this paper, we focus on the geological and compositional implications of color variations revealed in MDIS data. In the sections that follow, we first describe the acquisition and construction of the MDIS global color map. From those data we examine the relationship between smooth plains mapped globally by Denevi et al. (2013a) and older intercrater plains (Denevi et al., 2013b;

Table 1
Definition and description of color units described in this paper.

Unit name	Abbreviation	Typical values, current MDIS calibration			Description and characteristics	
		Reflectance at 750 nm, $i = 30°$, $e = 0°$, $g = 30°$	430–nm/1000–nm reflectance ratio, ratioed to global mean	PC2	Corresponding VIRS unit	Morphology
Low-reflectance material	LRM	0.04	1.1	0.03–0.04	Dark blue	Hummocky to lineated crater and basin ejecta; rims and central peaks
Low-reflectance blue plains	LBP	0.05	1.05	0.04	Average	Level at tens of kilometers, variable density of craters; commonly knobby
Intermediate plains	IP	0.06	1	0.045	Average	Level at tens of kilometers, variable density of craters; also in crater rims, ejecta within other plains units; spectrally equivalent to more heavily cratered unit previously called intermediate terrain (IT)
High-reflectance red plains	HRP	0.07	0.95	0.05–0.08	Average	Level at tens of kilometers, variable density of craters; also in crater rims, ejecta within other plains units
Red unit	–	0.08–0.14	0.8–0.9	0.06–0.08	Red	Diffuse low-relief haloes surrounding deep, scallop-rimmed depressions (interpreted as pyroclastic vents)
Fresh crater material	–	0.08–0.13	>1, to 1.3×	Not evident in PC2	Bright	Interiors, ejecta, and rays of Kuiperian-age craters
Bright hollows material	–	0.08–0.14	>1, to 1.3×	Not evident in PC2	Bright	Diffuse low-relief haloes surrounding shallow, flat-floored depressions (interpreted as erosional)

Notes: Nomenclature follows from Robinson et al. (2008) and Denevi et al. (2009). Content is from those references, Blewett et al. (2013), Braden and Robinson (2013), Goudge et al. (2014), and this paper. VIRS units are those of Izenberg et al. (2014). It is proposed here that the three plains units be prefaced by "smooth" or "intercrater" to describe their morphology distinct from their spectral properties.

Whitten et al., 2014). We then evaluate the presence and strength of absorptions or absorption-like features that may indicate localized pockets of iron-bearing silicate or the presence of specific darkening phases in LRM. Finally, on the basis of that evaluation, we model reflectance spectra of LRM and of the average northern hemisphere with a variety of candidate darkening components, and we assess whether required abundances are compatible with limits set by XRS and GRS measurements.

The MDIS global color map is complementary to globally distributed reflectance spectra over the wavelength range 0.3–1.44 μm that have been collected by MESSENGER's Mercury Atmospheric and Surface Composition Spectrometer (MASCS) Visible and Infrared Spectrograph (VIRS) (McClintock and Lankton, 2007). From those data, Izenberg et al. (2014) examined the same questions that we examine here with MDIS data. Compared with MASCS/VIRS spectra, MDIS/WAC multispectral image sets provide higher spatial resolution and continuous coverage, but the images sample the spectrum only through 11 discrete filters (of which eight have been used to construct the global map). MDIS is mounted on a pivot, enabling data to be collected at low emergence and phase angles, with a goal of also obtaining images at the smallest possible solar incidence angles. In contrast, VIRS is fixed to the spacecraft and constrained to view the surface at higher phase angles of 78–102°, commonly with either incidence or emergence angle having a high value. Analysis of MDIS data thus benefits from continuity of coverage, spatial resolution, and favorable viewing geometry, whereas the analysis of MASCS/VIRS data benefits from greater wavelength range and better spectral resolution.

2. Collection of the eight-color global map of Mercury

The MDIS/WAC global multispectral map is shown in Fig. 1a, normalized to a standard photometric geometry of 30° incidence angle, 0° emergence angle, and 30° phase angle. The majority of the data making up the map were acquired during the first Mercury solar day of MESSENGER's orbital mission, through 29 September 2011. Additional images to fill gaps were obtained during the mission's second Mercury solar day (through 26 March 2012). Imaging opportunities were selected to obtain a map with as uniform a spatial resolution as possible, at the lowest solar incidence angle available as a function of latitude, and at low emergence angles for accuracy in cartography. These goals had to be accomplished from a highly eccentric orbit (periapsis altitude ~200–500 km, apoapsis altitude ~15,000 km) that was not Sun-synchronous, so that illumination and viewing geometries were highly variable. Moreover, images required to complete the map were clustered in time when geometry was favorable, and were limited in both number and size by storage space on the spacecraft's solid-state data recorder and the downlink rate of the spacecraft telecommunications system.

To optimize the map within these constraints, the following approaches were used: (a) Images were acquired when the spacecraft ground-track was close to a noon–midnight geometry (i.e., when the planet–Sun line was close to MESSENGER's orbit plane), providing low incidence angles near nadir on the planet's day side. (b) Onboard 2 × 2 or 4 × 4 pixel binning was applied to images acquired at lower altitudes when the native spatial sampling of the images was better than several hundred meters per pixel, to control data volume while attaining an overall average spatial sampling of 1 km/pixel. (c) Also to control data volume, only eight of 11 spectral filters (Table 2) were used, sampling different parts of the spectrum at an average spacing in wavelength of ~110 nm. This spectral sampling is sufficient to detect and map ilmenite or Fe-rich olivine, pyroxene, or glasses if present in sufficient quantity, as well as differences in maturity resulting from space weathering. (d) The native 12-bit dynamic range of the data was compressed to 8 bits using a non-linear, information-preserving look-up table (Hawkins et al., 2007), and the resulting 8-bit data were compressed using wavelet techniques typically at a ratio of 3:1. Two subsequent regional multispectral imaging campaigns complement the eight-color map, but they are not analyzed here: a three-color map of northern and equatorial latitudes at an improved spatial sampling of ~400 m/pixel, and a five-color map of the northern volcanic plains (NVP). In addition 11-color image sets, acquired at lower altitude and higher spatial resolution, specifically target hollows, selected impact craters, and pyroclastic deposits. All 11 filters were used during the Mercury flybys.

Variations in illumination along the spacecraft ground-track resulted in two minima in incidence and phase angles, each approximately 30° west of Mercury's "hot poles" located at the equator at 0° and 180°E longitude (Fig. 1c). The median phase angle is near 45°, and the minimum is 28°. Extending out from the minima near the hot poles, opposite hemispheres have slowly varying photometric geometries; at the boundaries of the hemispheric coverage, higher phase angles and off-nadir geometries were required to attain continuity in coverage. As a result of the variations in illumination, there are large variations in apparent I/F in the data (where I is measured radiance and F is solar flux multiplied by π). Correction of the map to a standard photometric geometry requires an accurate model of the planet's photometric behavior. The model used here, described by Domingue et al. (2015), is based on southern-hemisphere portions of the map where there is overlapping coverage at a wide range of photometric geometries. The diversity in photometric geometries at which the same terrain is imaged supports normalization of measured I/F to that predicted at a standard geometry.

Acquisition of images for the eight-color map during the first Mercury solar day was clustered into four periods centered about 44 Earth days apart during which viewing conditions were most favorable. These images were acquired during the early stages of exposure of the spacecraft to thermal radiation from Mercury, which heated parts of the spacecraft to over 150 °C. For the first two weeks of orbital operations through 27 March 2011, during instrument commissioning, the MDIS pivot was kept in a "stowed" position (pointing cameras toward the spacecraft deck) to protect optics from any contaminants baked off of the spacecraft during initial orbital operations. About 8 weeks later, on 24 May 2011, the thermal environment first became hotter than during commissioning. Image data show that sensitivity of the WAC through all eight filters dropped abruptly by several to more than 10% and then slowly recovered over a period of months (Keller et al., 2013). Simultaneously on 24 May 2011, the electrical current required for cryogenic cooling of the GRS increased abruptly (J.O. Goldsten, personal communication, 2013). Both events are thought to have resulted from a contaminant that baked off the spacecraft, was redeposited onto cooler instrument surfaces, and then ablated over the following several months. Keller et al. (2013) developed an empirical correction for the resulting time-variable calibration of the WAC, tracking recovery of the camera's sensitivity using images of IP within a narrow, 5° window of incidence, emergence, and phase angles, which should yield a closely similar median I/F. The time-variability of the radiometric calibration was modeled as a temporal correction to calibration coefficients for the instrument, as explained in data set documentation archived with the NASA Planetary Data System (Murchie, 2013).

Because of effects contributed by the data collection strategy, the contamination event, and the inherent optical performance of the WAC, there are three noteworthy limitations to interpreting the eight-color map. First, the geometries used to develop the

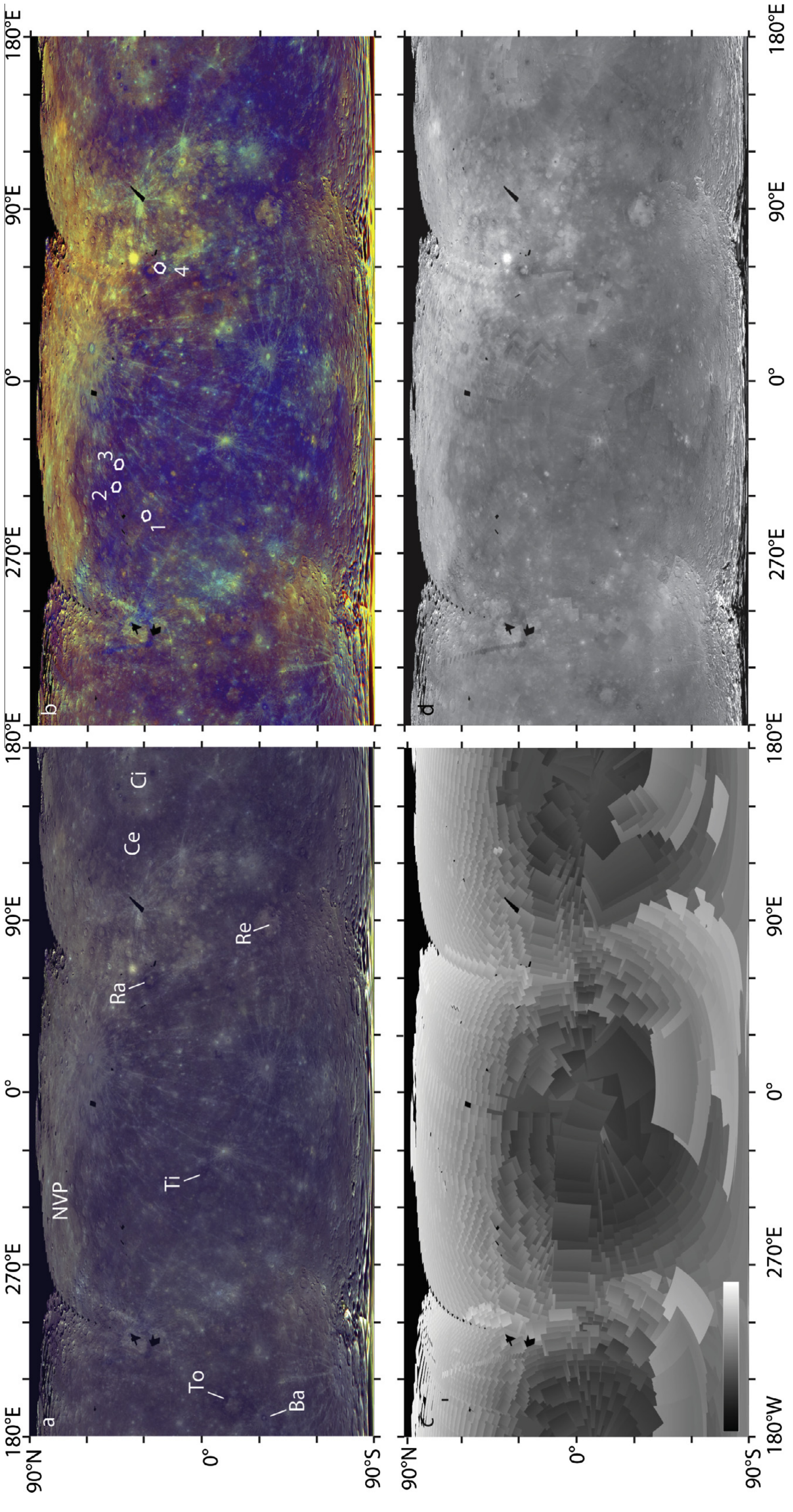

Fig. 1. A global overview of the MDIS eight-color map of Mercury. (a) Red–green–blue composite with red intensity set equal to the reflectance at 1000 nm, green intensity to reflectance at 750 nm, and blue intensity to reflectance at 430 nm. The linear stretches applied are red = 0.0–0.27, green = 0.02–0.21, and blue = 0.05–0.17. NVP = northern volcanic plains, To = Tolstoj, Ba = Basho, Ti = Titian, Ra = Rachmaninoff, Re = Rembrandt, Ce = Caloris exterior plains, Ci = Caloris interior plains. (b) Red–green–blue composite with red = PC2, green = PC1, and blue equal to the ratio of reflectance at 430 nm to that at 1000 nm. The linear stretches applied are red = 0.02–0.10, green = 0.10–0.25, and blue = 0.27–0.73. HRP appears orange and LRM dark blue. The white numbered circles show the locations of four XRS spectra of LRM acquired during solar flares. (c) Phase angle of images in the mosaic. The linear stretch ranges from 0° in black to 90° in white; the actual range in areas covered is 28°–90°. (d) PC2 values. High values of PC2 collocate with HRP and low values with LBP and LRM. The linear stretch ranges from 0.0 to 0.08. These and other maps in this paper are in simple cylindrical projection.

Table 2
Characteristics of the 11 MDIS WAC spectral filters, their approximate central wavelengths, and whether they were used as part of flyby observations, orbital targeted observations, the eight-color map, or subsequent three- and five-color maps.

Numerical/letter designation	Central wavelength, nm	Approximate central wavelength[a]	FWHM[b], nm	Targeted, flybys	Eight-color	Five-color	Three-color
6/F	433.2	430	18.1	x	x	x	x
3/C	479.9	480	10.1	x	x		
4/D	558.9	560	5.8	x	x	x	
5/E	628.8	630	5.5	x	x		
1/A	698.8	700	5.4	x			
7/G	748.7	750	5.1	x	x	x	x
12/L	828.4	830	5.2	x	x	x	
10/J	898.8	900	5.1	x	x		
8/H	947.0	950	6.2	x			
9/I	996.2	1000	14.3	x	x	x	x
11/K	1012.6	1020	33.3	x			

[a] Values typically cited in publications describing MDIS images and mosaics.
[b] Full width, half maximum.

version of the photometric correction applied here do not include a combination of high incidence and high emergence angles. Parts of the eight-color map acquired at those geometries – in the polar regions and at seams in the mosaic – may have residual, uncorrected photometric artifacts (Domingue et al., 2015). Second, the empirical correction for the contamination event is filter-dependent. Valid spectral "features" that may be present in Mercury's spectrum should therefore appear across multiple filters and correlate with geologic units. Third, WAC optical surfaces scatter light in a wavelength-dependent fashion: the point spread function is broader at long wavelengths than at shorter wavelengths. Longer-wavelength light is preferentially scattered out of small, bright features, potentially causing their apparent spectral reflectance to decrease at wavelengths >600 nm in a manner that could mimic a crystal field absorption due to olivine (Hawkins et al., 2009). Therefore spectral interpretation of small features should be confirmed by comparing results from MDIS images at different spatial resolutions, or with MASCS/VIRS spectra.

3. Data reduction and analysis

3.1. Mosaic construction

The following processing steps were applied to MDIS WAC eight-color image sets to produce a global map. (a) Data were calibrated to radiance by means of standard, filter-dependent calibration procedures, including dark current subtraction, dividing by a flat field, and multiplication by calibration coefficients to convert raw units to radiance. (b) Radiance was converted to I/F by dividing by the product of π and the solar flux scaled to Mercury's distance from the Sun. The model of solar flux used was that of Kurucz (1997). (c) I/F was normalized to reflectance at an incidence angle of 30°, an emergence angle of 0°, and a phase angle of 30° using the photometric model and parameters described by Domingue et al. (2015). (d) Images in each set acquired through all eight filters were co-registered to the 750-nm image within the set, and the image set was pruned to the region covered by all eight of the filters. (e) The resulting image "cubes" were map-projected onto an uncontrolled mosaic under the assumption of a spherical planet with a radius of 2440 km. To determine the stacking order of the final mosaic, i.e., which image is "on top," for each image set the term $PIXEL\_SCALE/[(\cos i)(\cos e)]$ was evaluated at the boresight of the 750-nm image, where i is incidence angle, e is emergence angle, and *PIXEL_SCALE* is the mean diameter of a projected pixel. The lower limit for *PIXEL_SCALE* was set to 665 m (even for images with higher native resolution), so that unfavorably illuminated images with high spatial resolution would not overwrite more favorably illuminated images. The image set having the highest value of the above expression was laid into the mosaic first, then the set with the second-highest value, and so on until the "best" set with the lowest value was on top.

3.2. Spectral mapping

Spatial variations in spectral properties were analyzed in the completed mosaic with two approaches. To search for absorptions due to potential Fe^{2+}-bearing mafic minerals, sulfides, and candidate darkening phases, three-point band depths were calculated using the methods of Clark and Roush (1984):

$$BD = 1 - [R_2/(aR_1 + bR_3)] \tag{1}$$

where BD is the depth of a particular absorption, and R_1, R_2, and R_3 are reflectance values at short, intermediate, and long wavelengths, and a and b are weighting coefficients. For a three-point band depth, R_1 and R_3 are reflectance values on the shorter- and longer-wavelength shoulders of the absorption, and R_2 is reflectance near the center of the absorption. The depth of a 1-μm band was calculated in a one-sided fashion, as:

$$BD = 1 - [R_3/(R_2 + \Delta(\lambda_3 - \lambda_2))] \tag{2}$$

$$\Delta = (R_2 - R_1)/(\lambda_2 - \lambda_1) \tag{3}$$

where here R_1 and R_2 are reflectance values at two shorter wavelengths outside the absorption that are used to define a continuum, λ_1 and λ_2 are the corresponding wavelengths, and λ_3 and R_3 are center wavelength and reflectance within the absorption. Band depth calculations are summarized in Table 3; all continua, expressed versus wavenumber, were fit by a line.

The artifacts discussed at the end of Section 2 create percent-level systematic differences in absorption depths between map-projected eight-filter image sets. To represent spectral variations in a cleaner fashion, we also performed a principal component analysis. Principal component 1 (PC1) represents underlying reflectance variations regardless of origin. PC2 (Fig. 1d) represents the variation in spectral slope and curvature between LRM and HRP, with the two end members having low and high values of PC2, respectively. Higher-order principal components contain both image artifacts and differences in maturity and were discarded. To show compositional and maturity variations, we instead constructed an enhanced-color composite that includes PC1, PC2, and a ratio of reflectance at 430 nm to that at 1000 nm, the last as a proxy for optical maturity (Fig. 1b). This product is consistent with previous color composites by Robinson et al. (2008) and Denevi et al. (2009) derived from flyby imaging.

Table 3
Spectral parameters used for mapping absorption band depths from MDIS images.

Parameter	Type	R_1, R_2, R_3 (nm)	Phase tested	Comments
BD480	3-point	430, 480, 550	FeS	Below detection limit of MDIS (⩽2% depth)
BD550	3-point	480, 550, 830	CaS	Below detection limit of MDIS (⩽2% depth)
BD630a	3-point	480, 630, 830	MgS, MnS, (graphite, ilmenite)	Broad band detected
BD630b	Hybrid 3-point	See comments	Graphite, ilmenite	Center wavelength average of 550, 630, 750, 830 nm; continuum tied to 480, 900 nm; broad band detected
BD900	1-sided	430, 630, 900	Low-Ca pyroxene	Below detection limit of MDIS (⩽2% depth)
BD990	1-sided	430, 630, 990	High-Ca pyroxene, olivine	Below detection limit of MDIS (⩽2% depth)

3.3. Spectral mixture modeling

For selected candidate darkening phases, we conducted spectral modeling to assess whether the phases could be responsible for darkening LRM. We made a simplifying assumption that space weathering is similar in its effects, though not necessarily in its rate, on different materials. We modeled the addition of each candidate opaque component to an end-member sample of HRP from the NVP that is already space weathered, to determine if mixing that phase together with HRP could reproduce the spectrum of LRM. To do the modeling, photometrically corrected MDIS reflectance spectra and spectra of laboratory analog materials, all acquired at $i = 30°$, $e = 0°$, and phase angle $g = 30°$, were converted to single-scattering albedo (SSA) following the procedures of Mustard and Pieters (1989). The equations of Hapke (2012) were used to combine SSAs using weight percent abundances, area-weighted by particle sizes and mineral densities. Standard densities were assigned to the minerals, and the density of NVP material was assumed to be 3 g/cm^3. Grain sizes for the NVP component were varied between 20 and 80 μm on the basis of prior estimates of regolith grain size. The optically dominant size range for lunar soils is 10–45 μm (Pieters, 1993). The average regolith grain size measured in returned lunar samples is ~70 μm (McKay et al., 1991), whereas Warell (2004) suggested that Mercury's regolith grain size is about half that of the Moon. Thus, average grain sizes of 20–80 μm for NVP material probably bracket the actual value. Grain sizes for the darkening component were varied between 2 and 20 μm. A smaller grain size for the darkening component is consistent with textures observed in partial melting experiments of the enstatite chondrite Indarch. In those experiments, sulfides that remained with the silicate melt were ~1–2 μm in size, compared with enstatite grains of 20 μm or greater (McCoy et al., 1999). Similarly, ilmenite grains in the lunar regolith are typically much smaller than silicate grains and are only a few micrometers in size (Heiken and Vaniman, 1990). Binary mixtures were simulated in steps of 1 wt% of the darkening component. Bidirectional reflectance for each mixture was computed at $i = 30°$, $e = 0°$, and $g = 30°$ with Hapke's equations. For a given combination of grain sizes, we found the mixture that minimized the sum of the squared difference from the target reflectance spectrum:

$$SS = \sum_{i=1}^{N} (R_{o,i} - R_{m,i})^2 \tag{4}$$

where SS is the sum-of-squares, $R_{o,i}$ is the observed reflectance at wavelength i, and $R_{m,i}$ is modeled reflectance at wavelength i. Results are shown in Table 4. The required mass fraction was then evaluated in light of elemental abundance measurements from XRS and GRS.

Table 4
Particle sizes and mass fractions of ilmenite and graphite required to darken NVP to match spectral reflectance properties exhibited by LRM in the ejecta of Rachmaninoff basin and exhibited by the average northern hemisphere, respectively.

Darkening phase	NVP particle size, μm	Darkening phase particle size, μm	Rachmaninoff LRM mass fraction	Ave. N. hemisphere mass fraction
Graphite	20	20	0.53	*0.08*
	20	10	0.36	**0.04**
	40	10	0.22	**0.02**
	40	2	0.05	**0.01**
	80	10	0.12	**0.01**
	80	5	0.07	**0.01**
Ilmenite	20	20	*0.90*	*0.23*
	20	10	*0.83*	*0.13*
	40	10	*0.70*	*0.07*
	40	2	*0.32*	**0.01**
	80	10	*0.54*	*0.04*
	80	5	*0.37*	**0.02**

Notes: Boldface indicates elemental abundances that are consistent with XRS or GRS limits; italics correspond to elemental abundances outside XRS or GRS limits. There are not yet constraints on carbon abundance at the scale of Rachmaninoff ejecta.

4. Results and discussion

4.1. Global overview

An overview of the spectral variations seen in the MDIS WAC eight-color map is shown in Fig. 1. Recognized units are summarized and described in Table 1. Materials with high values for PC2 (i.e., resembling HRP spectrally) are unevenly distributed across Mercury's surface. Conspicuous areas of high PC2 include previously recognized large deposits of HRP, specifically the NVP (Head et al., 2011), plains interior to the Caloris and Rembrandt impact basins, and scattered patches of smooth plains, plus the bright haloes of pyroclastic deposits such as the large occurrence northeast of the Rachmaninoff impact basin. To first order, these locations represent all but one of the largest occurrences of smooth plains mapped by Denevi et al. (2013a), plus the "red unit" haloes surrounding pyroclastic vents (Kerber et al., 2009, 2011; Prockter et al., 2010; Goudge et al., 2014). Scattered small patches of high-PC2 material also occur throughout the IP; most correspond to impact crater ejecta, which are interpreted to expose HRP buried by overlying volcanic IP (Ernst et al., 2010). In addition, a large area of intercrater plains at southern mid-latitudes from 220°E to 260°E longitude exhibits high values of PC2 and resembles HRP spectrally. Conversely, the lowest-PC2 materials represent LRM and occur in rims and ejecta of impact craters and basins. The most conspicuous deposit of LRM surrounds Rachmaninoff, and the largest deposits surround the basins Tolstoj and Rembrandt. Most of the surface consists of plains having intermediate values of PC2 and forming the IP and LBP units.

High-reflectance units other than pyroclastic deposits are undistinguished in the PC2 map. Reflectance variations associated with fresh crater materials are included instead in PC1, and variations in spectral continuum associated with crater rays are grouped with image artifacts into the higher-order principal components. In Fig. 1b, fresh crater materials including crater rays are identified instead by higher values in the 430-nm/1000-nm reflectance ratio. Bright, relatively blue materials associated with hollows have low values of PC2 that do not distinguish them from LRM and LBP despite their higher reflectance. This distinction is consistent with characterization of these materials from flyby data (Robinson et al., 2008) and with the finding by Blewett et al. (2013) that bright hollow materials are closely associated spatially with LRM. Compared with LRM, the reflectance of bright hollows materials is greater only by a few to nearly 10% (to ~0.14 at 750 nm at $i = 30^\circ$, $e = 0^\circ$, $g = 30^\circ$). Their spectral slope is reduced in a manner similar to that of fresh crater materials.

Comparison of color maps in Fig. 1a and b with phase angle coverage in Fig. 1c suggests that there may be uncorrected photometric effects in some regions imaged at high phase angles. Surrounding the phase angle minimum in each hemisphere, there is little or no systematic variation with photometric geometry. However, high-phase angle boundaries of coverage of each hemisphere, as well as polar regions observed at high phase and emergence angles, appear to be systematically reddened and consequently to have higher PC2 values. These trends are illustrated in Fig. 2a and b, which show the 430-nm/1000-nm reflectance ratio and PC2 as functions of phase and emergence angles. Phase angles $g > 70^\circ$ exhibit systematic reddening, whereas emergence angles $e > 20^\circ$ exhibit reduced spectral contrast. To ensure conservative interpretation of MDIS color imaging and avoid artifacts in subsequent analysis of plains units and LRM, the limits $g \leqslant 70^\circ$ and $e \leqslant 20^\circ$ were applied as masks to the data (Fig. 2c).

These results agree with those from analyses of spectral variations in the MASCS/VIRS data set reported by McClintock et al. (2008) and Izenberg et al. (2014): (a) the NVP and "red unit" are one spectral end member among major surface units, and LRM is the other; (b) most of the surface, consisting of other deposits of HRP, IP and its spectral equivalent IT, and LBP, lies along a continuum of variation between those two end members; and (c) fresh crater and bright hollows materials lie along a secondary spectral trend. Furthermore, the two data sets reproduce regional color variations. The correspondences between the data sets include features outside of basin-filling deposits: the relatively low-PC2 values around both equatorial hot pole regions at 0° and 180° longitude, the cluster of high-PC2 plains at northern latitudes around 90°E longitude corresponding to smooth plains deposits, and high-PC2 values of southern hemisphere intercrater plains around 240°E longitude. These correspondences between data sets preclude large-scale color variations in photometrically masked MDIS data from having originated as artifacts of radiometric calibration or photometric correction.

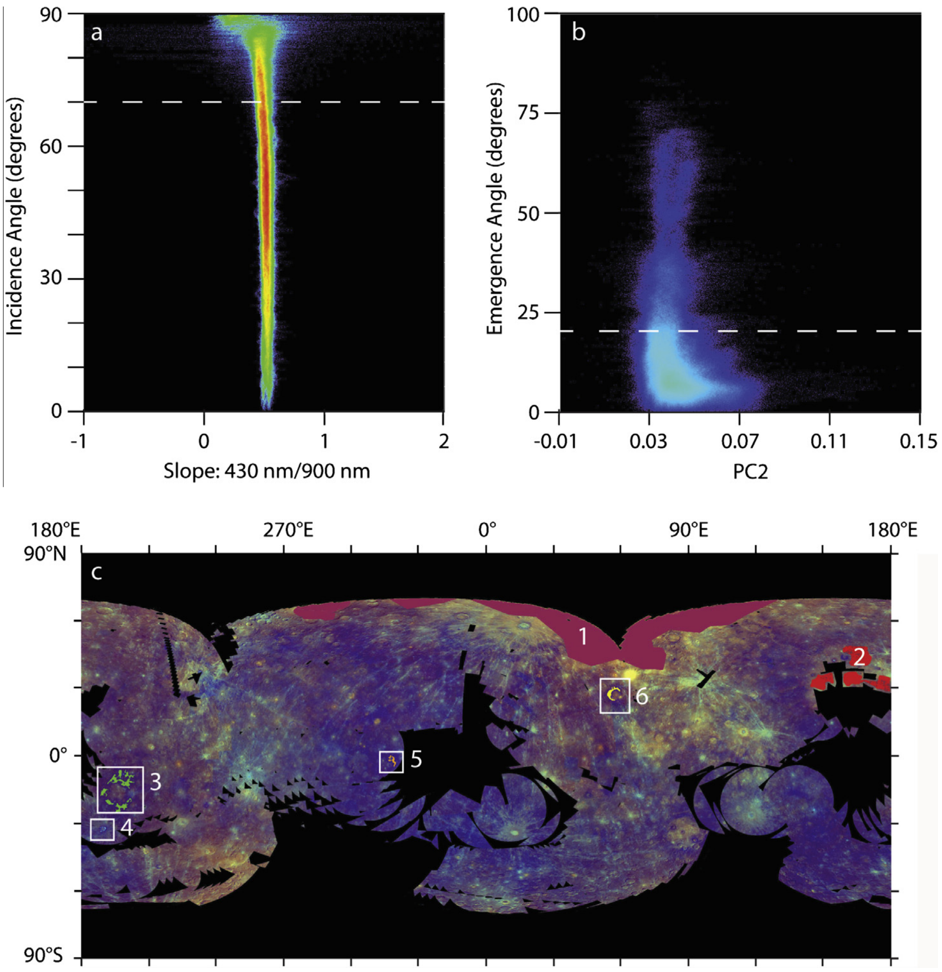

Fig. 2. (a) Two-dimensional histogram (rainbow color scale) of incidence angle versus spectral slope for 20 km × 20 km areas in the global color mosaic. Red indicates the highest density of points and blue the lowest. At incidence angles above 80°, spectral slope becomes increasingly affected by uncorrected incidence angle effects. Data acquired at an incidence angle >70° (white dashed line) were excluded from further analysis. (b) Two-dimensional histogram of emergence angle versus PC2 value. At emergence angles above ~25°, PC2 shows little variability. A threshold of $e \leqslant 20^\circ$ (white dashed line) was selected for spectral analyses. (c) Red–green–blue composite with red = PC2, green = PC1, and blue equal to the 430 nm/1000 nm reflectance ratio, with areas of high incidence and emergence angles masked. White numbered areas are regions of interest, including (1) an example area of HRP in the northern plains used as the denominator in spectral ratios and as the HRP end-member for mixture modeling, (2) a second example in Caloris, and LRM in (3) Tolstoj, (4) Basho, (5) Titian, and (6) Rachmaninoff.

4.2. Color variations among plains units

Intercrater plains are the dominant morphologic unit on Mercury. They have been described as being comparably level to smooth plains on a tens-of-kilometer scale, but with a higher density of superposed, mostly secondary craters than on smooth plains (Trask and Guest, 1975). Intercrater plains are less heavily cratered than the lunar highlands, particularly by craters <40 km in diameter, suggesting that they are younger and a product of widespread or global resurfacing (Strom and Neukum, 1988). On the basis of Mariner 10 data, the nature of intercrater plains resurfacing was controversial, with some authors favoring impact melt or fluidized ejecta from large basins (Wilhelms, 1976; Oberbeck et al., 1977) and others extrusive volcanism (Strom et al., 1975; Dzurisin, 1978; Malin, 1976).

MESSENGER data support the conclusion that many intercrater plains had a volcanic origin. Whitten et al. (2014) examined the morphology, elevation, and crater densities of intercrater plains that were mapped previously from Mariner 10 images. They concluded that intercrater plains are dominantly volcanic, and represent a more heavily cratered equivalent to smooth plains, because: (a) intercrater plains have a systematically greater crater density than smooth plains; (b) they are distributed globally rather than only surrounding large impact basins; and (c) there are numerous examples of secondary crater fields on smooth plains that create a textured morphology like that of intercrater plains. Denevi et al. (2013b) examined a Caloris-basin-sized region ~1500 km in diameter, identified by Fassett et al. (2012) as a probable degraded basin. They found that that IP-colored intercrater plains (IT) infill the basin interior and contain numerous superposed craters that excavated underlying HRP, that the basin rim is the site of pyroclastic vents as is the rim of Caloris basin (Murchie et al., 2008), and that the basin is centered on a gravitational low and has smooth plains at its center. They interpreted this occurrence of intercrater plains to be old, cratered IP emplaced volcanically or as fluidized ejecta burying even older HRP that infills a buried basin.

The global color map allows the first systematic global comparison of color properties of smooth and intercrater plains. Although color properties are not by themselves diagnostic of emplacement mechanisms, they may support one or another mechanism. To evaluate color properties of smooth and intercrater plains, we used the photometric angle masks described above, and measured the distribution of values of PC2 within smooth plains deposits mapped by Denevi et al. (2013a) and within other areas not mapped as smooth plains. Smooth plains were divided into NVP, HRP plains interior to Caloris, the exterior annulus of LBP plains surrounding Caloris, and all other smooth plains. The remaining deposits are grouped. They are dominated by intercrater plains, but they also include some contribution by LRM. On morphological grounds, the boundaries between terrain types are gradational. The results are shown in Fig. 3.

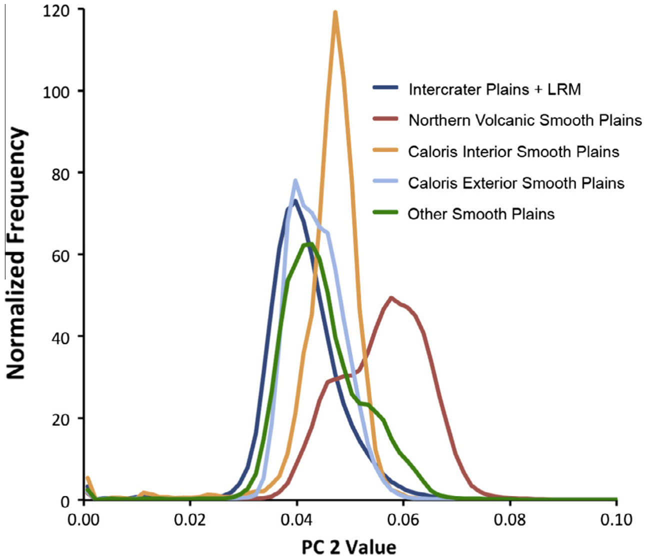

Fig. 3. Area-normalized histograms of the absolute values of PC2 in different occurrences of smooth plains and older areas, mapped with the unit definitions of Denevi et al. (2013a), within areas masked for incidence and emergence angle as shown in Fig. 2. Northern plains, Caloris interior plains, and Caloris exterior plains represent the three largest spatially contiguous occurrences of smooth plains.

There are both differences and similarities in the distributions of color properties within smooth plains and older areas as shown in Fig. 3. Among smooth plains, the NVP have distinct color properties, as indicated by the small amount of overlap between the distribution of PC2 values in NVP and those in other smooth plains units. However there is a low-PC2 shoulder to the histogram; thus, the NVP are not all uniform in color, and some are more typical of IP in their color. PC2 values in the Caloris interior plains are on average lower than in NVP but higher than in other smooth plains deposits, and overall they lie on the boundary between HRP and IP. Excepting the NVP and Caloris interior plains, PC2 distributions in other smooth plains deposits are similar to those in areas that include both intercrater plains and LRM. The two major differences are that the grouping of intercrater plains and LRM contains a low-PC2 tail that corresponds to the LRM, whereas remaining smooth plains have a high-PC2 shoulder that represents smooth HRP within Rembrandt basin and southwest of Caloris. Excluding LRM, the intercrater plains contain the spectral equivalents to all three of the smooth plains spectral units, HRP, IP, and LBP. In early interpretations of images from MESSENGER's first Mercury flyby of the Caloris interior plains and high-PC2 smooth plains southwest of Caloris, Head et al. (2008) and Murchie et al. (2008) interpreted distinct color properties to be one of the characteristics of smooth plains. Further work, for example by Denevi et al. (2013a) and in this paper, however, showed that other examples of smooth plains are commonly not as distinct spectrally.

Two insights into plains formation come from considering these results together with those of previous studies. First, the two largest smooth plains deposits (the NVP and Caloris interior plains) share color and morphologic properties that differ from the average properties of other mapped smooth and intercrater plains. Three large deposits account for over 80% of smooth plains: the NVP, the Caloris interior plains, and the annulus of plains exterior to Caloris (Denevi et al., 2013a). The NVP and Caloris interior plains exhibit morphologic characteristics strongly indicative of a volcanic origin, including embayment of high-standing topography, association with volcanic vents, and presence of flow features (Murchie et al., 2008; Head et al., 2008, 2009a,b, 2011; Fassett et al., 2009; Byrne et al., 2013; Denevi et al., 2013a). They also both have distinctly higher PC2 than most other smooth and intercrater plains (they belong to the HRP unit). Both the NVP and Caloris interior plains also lack craters <60 km in diameter exhibiting partial burial with preserved rims (Head et al., 2011; Ernst et al., 2015). Instead, identified pre-plains craters in that diameter range in the NVP are completely buried and form "ghost craters" marked by wrinkle-ridge rings or arcuate graben over the former rims (Klimczak et al., 2012). These observations have been interpreted to indicate rapid emplacement of volcanic materials >1 km thick by flood volcanism (Head et al., 2011; Ernst et al., 2015). Flood volcanism in the NVP is also supported by the nearby occurrence of large channels carved by flowing lavas (Byrne et al., 2013; Hurwitz et al., 2013).

In contrast, the Caloris exterior plains, the third major smooth plains deposit, are not similarly distinguished by high values of PC2. They are below average in reflectance and PC2 (they belong to the LBP unit) and show conflicting evidence for volcanism. Denevi et al. (2013a) found that portions of the Caloris exterior plains could also be interpreted as fluidized basin ejecta, on the basis of a knobby surface texture, gradation into Caloris rim deposits, lack of wrinkle ridges typical of other large smooth plains deposits, and evidence for flow into Caloris' interior, with the termini of flow features embayed by the interior plains.

A second insight is that, in contrast to the two large HRP deposits, other, generally smaller deposits of smooth plains are strongly similar in their range of color properties to intercrater plains. Like smooth plains, intercrater plains also exhibit regional heterogeneity in color, in particular a high-PC2 region in the southern hemisphere near 240°E that shares the spectral characteristics of HRP but is more heavily cratered. Ernst et al. (2010) showed that in IP, some craters exhume HRP from depth, for example, at the Titian and Homer basins. Similarly, Denevi et al. (2013b) showed that craters in IP also excavate HRP from depth. They interpreted these results to indicate burial of volcanic HRP materials by lower-reflectance IP emplaced volcanically or as impact basin ejecta.

In summary, excepting the Caloris interior plains and the NVP, color properties within smooth plains deposits resemble those within intercrater plains. Also, both smooth and intercrater plains exhibit interlayering of IP with HRP having color and reflectance characteristics resembling those of the NVP and Caloris interior plains. The distinction between smooth and intercrater plains is not color but instead crater density, consistent with previous suggestions that intercrater plains are an older equivalent to smooth plains (Malin, 1976; Strom et al., 1975; Dzurisin, 1978; Denevi et al., 2013a,b; Whitten et al., 2014).

Given these results, the nomenclature used for plains units warrants revision. Currently, IT is distinguished from IP on the basis of surface morphology despite similarity in reflectance and color. In contrast, spectral equivalents to HRP and LBP within intercrater plains are not distinguished. We suggest an alternative descriptive nomenclature for plains that separates morphologic and spectral properties, i.e., HRP, IP, or LBP prefaced by "smooth" or "intercrater" on the basis of the density of superposed craters. With this nomenclature, IT would be replaced by "intercrater IP."

4.3. Constraints on sulfide and silicate mineralogy

Band-depth mapping with MDIS multispectral data (summarized in Table 3) complements spectral mapping by MASCS/VIRS. We examined both the full-resolution MDIS orbital mosaic (rendered at 0.66 km/pixel, to preserve native resolution in parts of the mosaic with better spatial sampling) and also a median-filtered version of the mosaic subsampled to 20 km/pixel that has reduced radiometric artifacts and more precisely measures weak spectral variations.

The MDIS data reveal no clear evidence for deposits dominated by sulfides or Fe^{2+}-rich mafic minerals at 20-km scales. Depths of bands attributable to ferrous iron in pyroxene (parameter BD900 in Table 3) or olivine (BD990) show no enhancements in association with geologic features, outside of image artifacts attributable to scattered light or frame-to-frame residual differences in calibration. Band depths associated with sulfides (BD480, BD560, BD630a) do show weak enhancements within selected deposits of LRM. However, as explained below, the enhancements are a consequence of the sensitivity of these parameters to the broad 600-nm feature and do not constitute detection of the much narrower sulfide absorption features targeted by these parameters. Again, most variation is associated with image artifacts. The level of artifacts present in all five band-depth parameters varies regionally and is largest at seams in the mosaic, between coverage taken at different times or different photometric geometries. Globally, the upper limit on any absorptions contributed by ferrous-iron-containing silicates and Fe, Ca, Mg, and Mn sulfides in the MDIS eight-color map is approximately 2% over a 20-km spatial scale; in the best-resolved regions of the mosaic the upper limit is smaller by a factor of 2–3.

These results agree with constraints on band depths from the MASCS/VIRS data (Izenberg et al., 2014): (a) there is no evidence for a 1-μm absorption due to ferrous iron in olivine or pyroxene, within the limitations of those data, and (b) there is no evidence for absorptions due to sulfide phases, within spatial resolution and signal-to-noise ratio limitations of those data. Compared with MDIS data, MASCS/VIRS data provide more definitive constraints on weak ferrous iron or sulfide absorptions by virtue of the multiple spectral samples that VIRS obtains across each absorption band. Izenberg et al. (2014) used the MASCS/VIRS results to estimate upper limits on olivine, pyroxene, and sulfide abundances. The upper limit on 1-μm absorption band depth as measured by VIRS (~5%, 5 standard deviations) translates to an upper limit on FeO in silicates of 0.9%. The constraint on sulfide abundance is weaker; the upper limit of sulfide band depth (~1%, 5 standard deviations) only precludes resolvable occurrences of Mg and Ca sulfide minerals with abundances of ~70–80% or more.

4.4. Spectral heterogeneity of LRM

In contrast to the lack of narrow Fe^{2+} or sulfide absorptions, there is clear evidence in MDIS imaging for a broad, shallow absorption-like feature centered near 600 nm, which is recognized only in LRM. The 600-nm feature is mappable most clearly with the BD630b parameter (Table 3) and is consistent with the feature identified previously in multispectral images acquired during MESSENGER's Mercury flybys and attributed at that time to a possible Ti-bearing phase (Robinson et al., 2008; Denevi et al., 2009). It is strongest, with a depth of ~10%, in a subset of LRM deposits having the lowest values of PC2. For more detailed examination, we focused on areas of LRM sufficiently large to minimize scattered light artifacts, away from extreme photometric geometries, and where seams in the image mosaic are minimal. We also excluded deposits for which the multispectral images were obtained during the period shortly after the contamination event, when calibration artifacts were greatest.

Visualizations of four areas of LRM having a range of strengths in their 600-nm features, from near-zero to ~10%, are shown in Fig. 4. Fig. 5a–c shows MDIS spectra of these locations, as reflectance normalized to $i = 30°$, $e = 0°$, $g = 30°$, and also as spectral ratios relative to a reference area in the NVP (magenta region, Fig. 2) to enhance spectral contrast. The NVP was chosen as a reference because it is a high-HRP end-member and should have the lowest fraction of the LRM-darkening component. Not only are these examples of LRM all lower in reflectance than NVP, they are also all much less red, i.e., they are "bluer." This observation helps to constrain the characteristic of the component that darkens LRM.

The four LRM deposits overlap in reflectance but exhibit large differences in the depth of their 600–nm feature, showing that LRM is spectrally diverse despite the extreme blandness of other surface units at visible to near-infrared wavelengths. The deposits also exhibit a range of relative ages, described here using the stratigraphic system for Mercury of Spudis and Guest (1988) which uses five relative age groupings. The 600-nm feature is weak to absent in the ejecta of Tolstoj. This material surrounds the 510-km diameter impact basin (centered at 16.2°S, 195.3°E) and, at the stratigraphic boundary between pre-Tolstojan and Tolstojan-aged

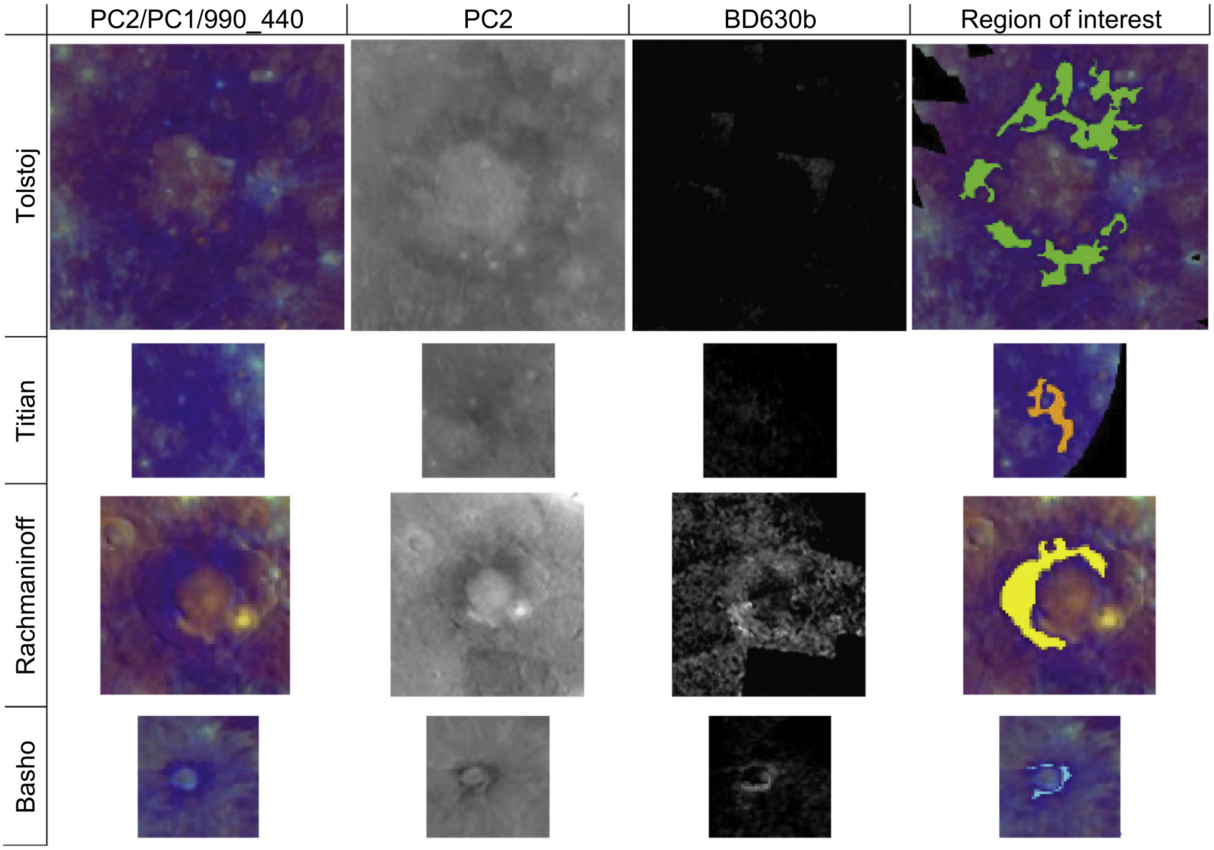

Fig. 4. Spatial variations in spectral properties of large LRM deposits in regions removed from extreme photometric geometries and mosaic seams. Top to bottom, LRM with decreasing exposure age: Tolstoj basin ejecta, LRM northeast of Titian, Rachmaninoff, and Basho. Left to right: false color composite with red = PC2, green = PC1, and blue equal to the 430-nm/1000-nm reflectance ratio (as in Figs. 1b and 2c); PC2; BD630b (see Table 3); and false color composite as in the left column, except indicating regions of interest for which spectra are plotted in Fig. 5. The stretches in the false-color composite and PC2 are the same as in Figs. 1b and 2c; the stretch for BD630b is 0.0–0.16.

materials, is the oldest and largest of the four LRM deposits in Figs. 4 and 5. The 600-nm feature is present but weak in LRM within ejecta of the crater Titian. Ejecta on the northeast rim of this 109-km diameter crater (centered at 3.7°S, 317.4°E) are superposed on an older, unnamed, HRP-filled basin. On the basis of this stratigraphic relation, the ejecta are probably Calorian in age, i.e., in the age group next younger than Tolstojan. The feature is strongest in the ejecta of Rachmaninoff and in rim materials of the crater Basho. The ejecta of Rachmaninoff (centered at 57.6°N, 27.8°E) exhibit secondary craters superposed on surrounding smooth plains, and the ejecta themselves are sparsely cratered but there is no sign of rays. These properties are consistent with a Mansurian age, belonging to the second youngest age group. Basho (centered at 32.4°S, 189.6°E) is a 75-km-diameter, Kuiperian-aged (i.e., in the youngest age group) crater that despite retaining rays also exhibits a strong LRM signature in its rim and wall materials. Among other, smaller regions we examined that are not shown here, qualitatively it appears that fresher exposures also have higher values of BD630b. The phase responsible for the absorption-like feature is considered further in Section 4.6, but of the phases examined, the only ones having a broad curvature centered near 600 nm are ilmenite, a form of carbon such as graphite (Fig. 6b), or a mixture of nanophase and microphase iron (Riner and Lucey, 2012).

We considered three hypotheses to explain variations in strength of the 600-nm feature among LRM deposits. (a) All freshly exposed LRM deposits exhibit a relatively strong 600-nm feature, but the absorption is weakened with time by impact mixing vertically with underlying IP or HRP, or horizontally with adjacent IP or HRP materials that lack the 600-nm feature. The similarity of reflectance between LRM deposits exhibiting a range in BD630b is inconsistent with this hypothesis, if it is supposed that all LRM originates with identical spectral properties. (b) LRM is exposed at the surface with a 600-nm feature that is degraded by space weathering processes. For example, a darkening phase with a 600-nm feature may be “overprinted” with a mixture of iron or iron sulfide that has different grain sizes formed by space weathering and that is spectrally neutral. This hypothesis may be consistent with the observed relation between BD630b and relative age, if space weathering has minimal effects on the overall reflectance of already dark materials. (c) LRM may contain two or more compositions, one with and one without a 600-nm feature, and different impact features excavate different materials. This explanation would require the presence of more than one darkening phase in the crust, such as graphite that does exhibit this feature and microphase metallic iron, which by itself does not (see Section 4.6). In this case, the apparent correlation of strength of the 600-nm feature with age would be an artifact of the small number of large exposures that meet our data quality criteria.

Similarities and differences among LRM deposits observed in MDIS data are reproduced in spectra measured by VIRS. Fig. 5d shows VIRS spectra of the same LRM materials for which MDIS spectra are shown in Fig. 5c, corrected photometrically to a standard geometry of $i = 45°$, $e = 0°$, and $g = 45°$, and normalized to NVP to minimize residuals from differences in the radiometric calibration or photometric correction of the two different data sets. In both data sets, Basho and especially Rachmaninoff exhibit a broad, deep 600-nm feature, whereas the spectra of Tolstoj ejecta are

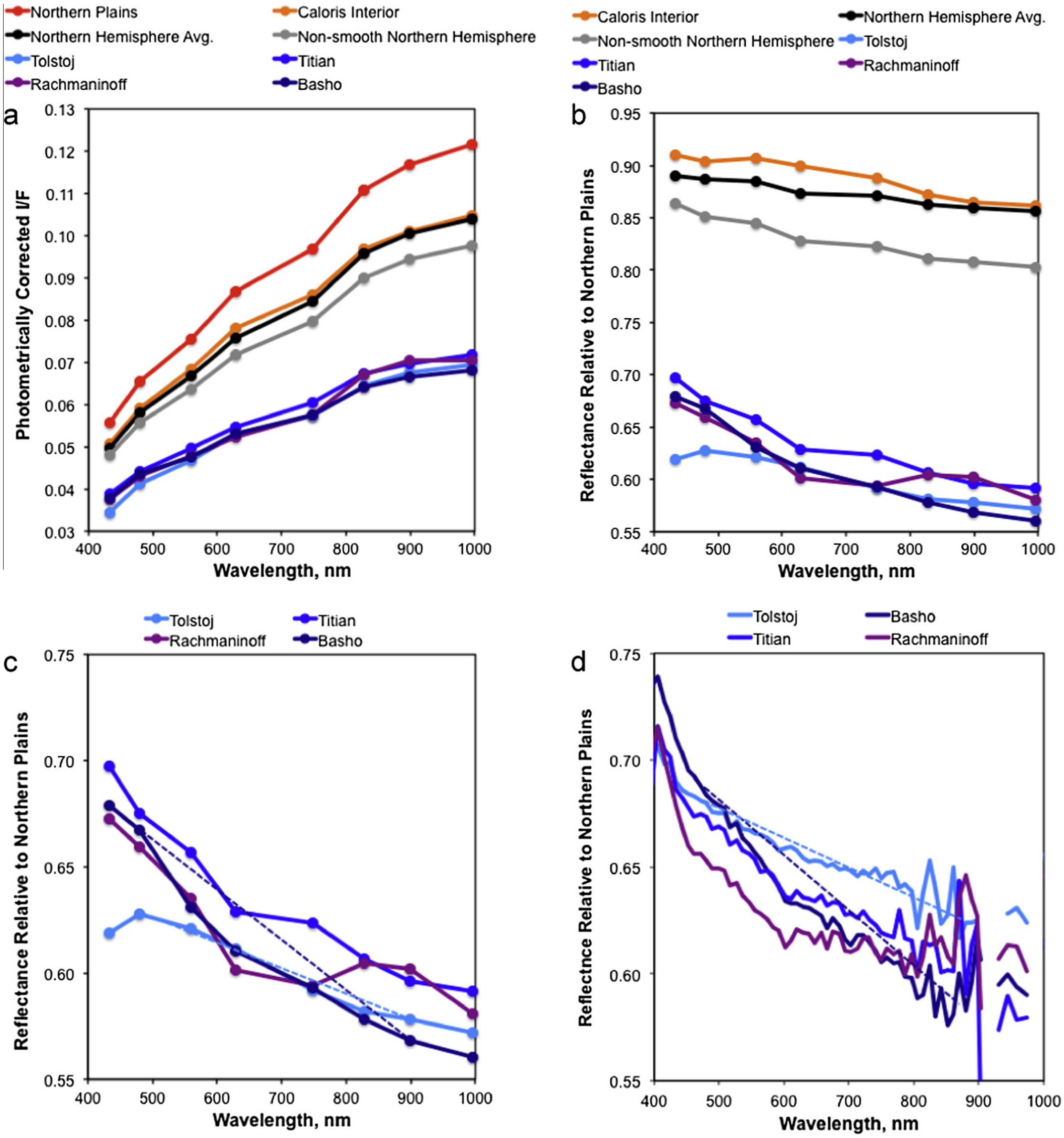

Fig. 5. Spectra of NVP, Caloris interior plains, average northern hemisphere, average non-smooth plains in the northern hemisphere, and the LRM deposits shown in Fig. 4. (a) *I*/*F* measured by MDIS, and corrected to 30° incidence angle, 0° emergence angle, 30° phase angle. (b) Same, ratioed to the NVP reference area. (c) LRM examples shown with an expanded scale to highlight differences among them. (d) Same LRM locations as in (c) except as measured by VIRS, corrected to 45° incidence angle, 45° emergence angle, 90° phase angle, and ratioed to measurements of the same NVP reference area. In (c and d), the dashed lines show straight-line continua over the 480- to 900-nm wavelength range used to calculate BD630b, for Tolstoj ejecta lacking the 600-nm feature (light blue) and Basho ejecta with a strong feature (dark blue).

nearly featureless. Also in both data sets, the overall reflectance levels of the four LRM deposits are closely similar.

4.5. Implications for LRM stratigraphy

We considered four hypotheses for formation of the low-reflectance component of LRM: (a) The dark material is an intrinsic component of deeply excavated basin material (e.g., Robinson et al., 2008; Denevi et al., 2009; Riner et al., 2009, 2010; Ernst et al., 2010). The observation that LBP and IP lie along a spectral continuum between LRM and HRP suggests but does not require that the same darkening component also occurs in the LBP and IP plains units. (b) A darkening component is produced gradually by space weathering, perhaps with spectral properties of the resulting material modulated by an endogenic opaque component envisioned in the first hypothesis. Lucey and Riner (2011) and Riner and Lucey (2012) modeled low-reflectance regions of Mercury as resulting from space weathering in which a mixture of nanophase and microphase (micrometer-sized) metallic iron is formed at the boundaries of silicate grains. Space weathering by formation of iron sulfides as seen on regolith grains from Asteroid Itokawa is also a possibility, but this possibility has not been explored in detail. (c) LRM is the ultimate product of space weathering and the most mature of all materials on Mercury, near the bottom of the stratigraphic column. (d) The darkening phase is predominantly exogenic in origin and contributed by bolides. Bruck Syal et al. (2015) argued that the diffuse nature of some LRM can be explained by deposition of carbon-bearing compounds from vaporized cometary impactors, and that meteoritic carbon is delivered to Mercury at a rate that over geologic time could be equivalent to a global layer of carbon meters in thickness.

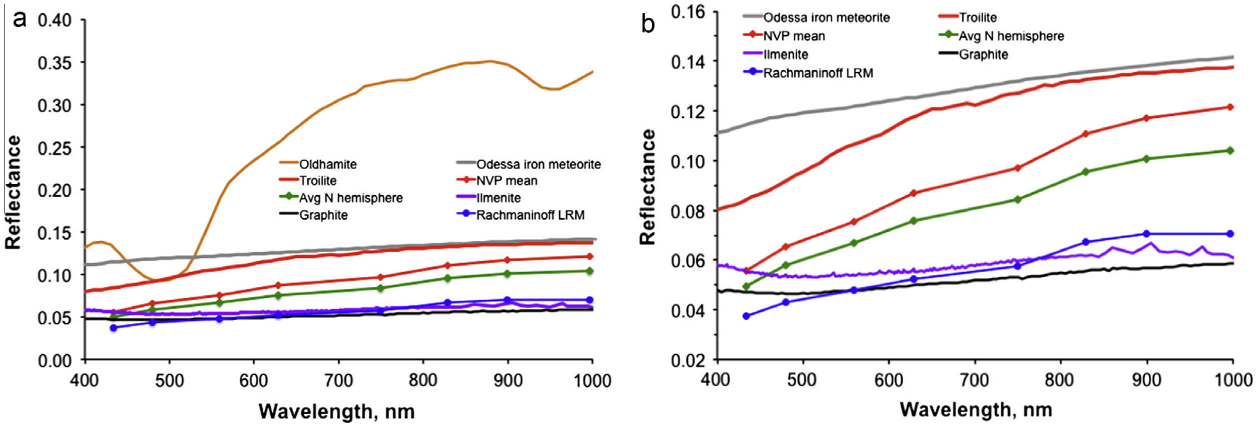

Fig. 6. (a) Laboratory reflectance spectra of candidate LRM components, compared with those of areas of Mercury corrected to the laboratory measurement geometry of $i = 30°$, $e = 0°$, and $g = 30°$ (reference area of the northern plains [NVP mean], average northern hemisphere material, LRM ejecta of Rachmaninoff basin). All analog materials have a particle size of 40 μm. (b) Darker analog materials with an expanded vertical scale to highlight shapes of the spectra.

Multiple lines of evidence support either or both of the first and second hypotheses, that the darkening phase in LRM is an intrinsic component of Mercury's crust and/or upper mantle, modified by gradual space weathering. Not all LRM has an extremely old exposure age, so it cannot be the ultimate product of space weathering. Deposits of LRM occur throughout the stratigraphic column, and some of the strongest LRM signatures occur in stratigraphically young, Mansurian- to Kuiperian-aged material. LRM occurs within Kuiperian rayed craters, showing that it occurs in locations where optical maturity has not developed on exposed surfaces. Neither the spatial distribution of LRM nor its chemistry is consistent with an origin entirely by bolides. The occurrence of sharp boundaries to LRM that correspond to morphologic unit boundaries such as impact crater rims and ejecta, plus the excavation of LRM from beneath plains units such as those interior to Caloris, are inconsistent with superposition of an exogenic darkening component. In addition, in Section 4.6 we show that several percent C are required to darken HRP to LRM. Peplowski et al. (2015) noted that the observed abundance of Fe is much lower than it would be if accompanied by C at abundance ratios comparable with those observed in carbonaceous chondrite meteorites. The same is true if the source of C was cometary material similar to that in Stardust returned samples (Brownlee et al., 2012). An origin of LRM intrinsic to Mercury is supported by the age relations described above, and by reflectances of young craters. Even the freshest, most recently exposed bright crater materials have only half the reflectance of comparable lunar highland materials, suggesting that an endogenic darkening phase is present on Mercury and is not restricted to LRM (Denevi and Robinson, 2008; Braden and Robinson, 2013).

4.6. Modeling the darkening component in LRM

In selecting candidate darkening phases in LRM and modeling their effects on spectral reflectance, we made five assumptions. First, we assumed that the NVP is representative of crustal material either lacking or with a low content of the darkening phase, on the basis of the observations that LRM and HRP appear to represent opposite ends of a spectral continuum. Second, we assumed that space weathering affects major color units of Mercury in a similar fashion (though not necessarily at the same rate), so that mature LRM can be modeled as an intimate mixture of mature HRP and a darkening phase. Third, because some LRM exhibits upward curvature of the spectrum centered at 500–650 nm, the darkening phase should also exhibit this feature. We were not strict about the shape of the absorption, however; for sulfides, Helbert et al. (2013) showed that heating of CaS, MgS, and MnS to Mercury's surface temperature can shift and broaden the absorption at 500–650 nm for these minerals. Fourth, the darkening component consists of compounds that could be present at least at the percent level and are compatible with a chemically reduced mineral assemblage such as that believed to characterize Mercury's surface (Nittler et al., 2011; McCubbin et al., 2012).

Fifth, on the basis of the stratigraphy of color units summarized above, we assumed that the phase darkening LRM is intrinsic to Mercury's crust as opposed to a product entirely of space weathering. Because most of the surface consists of volcanic materials (Head et al., 2008, 2009a,b; Denevi et al., 2009, 2013a,b), through which LRM has been excavated by impact, by this assumption LRM is taken to have formed as buried extrusive material, igneous intrusions, primary crust, or a differentiated layer of the upper mantle. Compared with extremely fine-grained (nanometer-scale) products of space weathering, candidate opaque minerals in such materials should be relatively coarse (but may still be much smaller than typical silicate grains). For instance, ilmenite grains in high-Ti lunar basaltic regoliths are tens of micrometers in size or larger, several times smaller than silicate grains (Heiken and Vaniman, 1990). Native iron can occur as an igneous mineral under extremely reducing conditions (e.g., Iacono-Marziano et al., 2012). Grains of metallic Fe in Greenland basalts are tens of micrometers to millimeters in size (Ulff-Moller, 1990; Iacono-Marziano et al., 2012); graphite in the same basalts is of micrometer size (Ulff-Moller, 1990). Rubin (1997) found that graphite in highly reduced melts within enstatite chondrites ranges in size from 1–2 μm to tens of micrometers. Our assumption of micrometer-sized or larger grains is critical; as shown below, excluding sub-micrometer sized grains precludes iron or iron sulfide from producing sufficient darkening to convert HRP into LRM.

Five phases were identified as candidates (Fig. 6). The first is ilmenite, $FeTiO_3$. Although XRS results place an upper limit of 0.8 wt% on the abundance of Ti averaged over large areas, whether the implied low abundance of ilmenite ($\leqslant$2.5%) could still darken Mercury's surface sufficiently to produce LRM has not been reevaluated. To model the effects of ilmenite, we used a spectrum of RELAB sample TB-TJM-038/C1TB38, shown by Blewett et al. (2013).

The second considered phase is oldhamite (Ca,Mg)S, which is present in enstatite chondrite and achondrite meteorites that have been invoked as possible analogs to the silicate fraction of Mercury (Lodders and Fegley, 1992; Burbine et al., 2002). Its presence has been suggested on Mercury on the basis of telescopic spectroscopy (Sprague et al., 1995) and elemental abundance correlations in XRS data (Weider et al., 2012). Different samples of oldhamite exhibit absorptions centered over the wavelength range 500–600 nm (Burbine et al., 2002; Blewett et al., 2013; Helbert et al., 2013). A range of reflectances has also been reported, and exposure to Mercury surface temperatures in the laboratory has been shown to lower the reflectance of the Ca and Mg sulfides as well as Mn sulfides (Helbert et al., 2013). The sample we used in spectral modeling (USGS sample HS231.3B) is darker than those of Helbert et al. (2013).

Third, troilite (FeS) has also been proposed as a surface constituent on the basis of XRS results and telescopic spectroscopy. It has been suggested to be a darkening component on some low-albedo asteroids with red-sloped spectra (Bus and Binzel, 2002). On the basis of analysis of returned Hayabusa samples, nanophase FeS on grain surfaces has been identified as a product of space weathering on the S asteroid Itokawa (Noguchi et al., 2011). RELAB sample TBRPB-005/C1TB05 was used for our spectral modeling.

Fourth, metallic iron occurring as a mix of nanophase to microphase grains has been proposed to darken surfaces on Mercury without reddening them (Lucey and Riner, 2011). Gillis-Davis et al. (2013) showed that impact shock and melting such as the processes that affected "shock-blackened" chondrite meteorites (Britt and Pieters, 1994) can also produce such mixtures. Such mixtures have also been proposed as a darkening agent in low-albedo outer Solar System materials (Clark et al., 2012). Scattering by a mixture of nanophase- to micrometer-sized grains leads to curvature in the visible spectrum not unlike that observed in LRM. We used a spectrum of a particulate sample of the Odessa iron meteorite (University of Winnipeg sample MET01A) to simulate a micrometer-sized component.

Fifth, some form of solid C, modeled here as graphite (RELAB sample SC-EAC-080/CASC80) has been discussed as a candidate darkening agent by Denevi et al. (2009), Blewett et al. (2009), and Bruck Syal et al. (2015). Ebel and Alexander (2011) suggested that Mercury's reduced composition may be the result of accretion from carbon-rich material. Geochemical modeling by Vander Kaaden and McCubbin (2015) indicates that during Mercury's differentiation, graphite would have been the stable form of carbon and the only phase lighter than bulk melt. They inferred that for this reason Mercury may have developed a primary flotation crust enriched in graphite. Presumably any such crust would subsequently have been mixed vertically with underlying intrusive material and overlying lavas by impact melting and brecciation and distributed through a much thicker layer during the late heavy bombardment. In highly reduced Greenland basalts in which carbon was assimilated into rising magma (e.g., Ulff-Moller, 1990; Iacono-Marziano et al., 2012), and in melts in enstatite chondrites (Rubin, 1997), graphite occurs as an igneous mineral at the half-percent level. The reflectance spectrum of graphite has a broad upward curvature centered at 500–550 nm (Cloutis et al., 2011) not unlike that in LRM.

MESSENGER's GRS is sensitive to carbon, but the signal of the spacecraft's carbon-composite structure has to be removed from GRS measurements to estimate the abundance on Mercury's surface. With current data reduction techniques, the estimate of C content averaged over the northern hemisphere is 1.4 ± 0.9 wt% (1-standard-deviation error). Because this estimate is insufficiently distinct from zero, it does not constitute a detection of C on Mercury, but it does place a 3-standard-deviation upper limit of 4.1 wt% on the abundance of C in average northern hemisphere surface material (Peplowski et al., 2015). No assessment of C abundance at smaller horizontal scales has been made.

Several other phases with absorptions centered at 600–700 nm were not considered, on the basis of geochemical considerations. Fe-rich phyllosilicates such as cronstedtite (Cloutis et al., 2011) and selected ferric oxides such as goethite (Morris et al., 1985) are oxidized and not consistent with a reduced mineral assemblage; also, there is no evidence in MASCS/VIRS spectra for a phyllosilicate metal–OH absorption near 1400 nm (Izenberg et al., 2014). Manganese sulfide (browneite), documented in enstatite achondrites by Ma et al. (2012), has been suggested as a possible darkening phase by Helbert et al. (2013). MnS has a suitable 600-nm feature, but XRS data constrain its abundance to be much less than 1% (Nittler et al., 2011).

If present as coarse, micrometer- or larger-sized grains, most of these phases are too bright to be the darkening agent in LRM. Fig. 6 compares laboratory spectra of ~40-μm-sized analog materials to spectra of NVP, all measured at or corrected to a geometry of $i = 30°$, $e = 0°$, $g = 30°$. Troilite and oldhamite are brighter than the NVP and thus not capable of providing the required reduction in reflectance. The sulfide spectra shown by Helbert et al. (2013) are even brighter and less suitable. This comparison does not preclude the presence of sulfides in LRM, or thermal decomposition of sulfides having a role in the formation of hollows (Blewett et al., 2011, 2013; Helbert et al., 2013). It does indicate, however, that the darkening phase is probably not coarse-grained sulfides, unless thermal processing can yield much greater darkening over geologic timescales than has been observed in the laboratory.

Coarse-grained metallic Fe is by itself incapable of darkening HRP to LRM. Large grains are too bright and would increase the reflectance of HRP (Fig. 6). However, a substantial component of added nanophase Fe could sufficiently darken HRP (Riner and Lucey, 2012), but it would also redden the mixture. The relatively "blue" nature of LRM provides a fundamental constraint on the proportions of coarser-grained (microphase) and nanophase Fe.

Of the coarse-grained phases considered here, both ilmenite and graphite can darken HRP to LRM. Table 4 shows, for various combinations of grain sizes, the mass fractions required to produce model spectra that fit the average spectrum of the northern hemisphere. That area is chosen because it corresponds to the area over which elemental abundances are constrained by GRS observations (Evans et al., 2012). In all cases, small grain sizes of the darkening phase are required, but such a requirement is not inconsistent with known natural occurrences as summarized above. Surprisingly, ilmenite can provide sufficient darkening to nearly reproduce the northern hemisphere average spectrum, without violating elemental abundance constraints, for cases in which the ratio of the grain size of NVP material to that of darkening material is $\geqslant 20$. For the grain size ratios examined, however, ilmenite would have to be present at 30 wt% to darken HRP to LRM. Such an abundance would be unexpected because petrologic modeling indicates that ilmenite cannot stably coexist with the low-FeO silicates implied by the lack of a 1-μm absorption (Riner et al., 2010).

The 0.8 wt% XRS upper limit on the surface Ti abundance reported by Nittler et al. (2011) was based on measurement footprints with large horizontal dimensions, mainly at southern latitudes. Such a consideration raises the question as to whether smaller regions of LRM could have higher Ti abundances. Multiple years of orbital data collection have led to a substantial number of spatially resolved XRS measurements in the northern hemisphere during solar flares, when elements heavier than Si can be detected (e.g., Weider et al., 2012, 2014). We searched the XRS database for measurements during solar flares for which the instrument footprint mainly included LRM and identified four such spectral integrations with sufficiently high signal-to-noise ratios to determine limits on the Ti abundance (the four areas outlined in white in Fig. 1b). One of the XRS footprints covers Rachmaninoff ejecta (area 4 in Fig. 1b); the spectrum (summed over the three XRS detectors) for this measurement is shown in Fig. 7. The spectra for all four LRM-rich footprints were analyzed following procedures described by Nittler et al. (2011), and none showed evidence

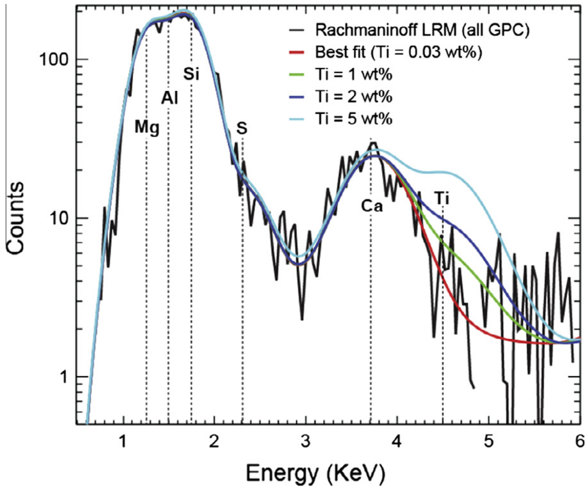

Fig. 7. XRS spectrum (black) of LRM in the southeastern ejecta of Rachmaninoff basin, compared with theoretical spectra corresponding to the best-fit elemental composition and different Ti contents. The background-subtracted, 40-s-integration spectrum was acquired at 15:38:47 UTC on 30 July 2012 and is the sum of the three gas proportional counter (GPC) detectors. The best-fit model (red) has 0.03 wt% Ti, and values ⩾1 wt% are inconsistent with the data. Energies of major elemental fluorescence lines are indicated by vertical dashed lines.

for high Ti. For the measurement of Rachmaninoff ejecta, the best fit to the data is for a Ti abundance of 0.03 wt%. Comparing theoretical spectra with higher Ti abundances to the observed spectrum (Fig. 7) clearly rules out values higher than ~1 wt%; a similar bound is seen for the three other measurements. These results rule out ilmenite or a related phase being present at levels of tens of wt% in LRM. Thus, although ilmenite may be capable of darkening surfaces, it cannot account for the low reflectance of LRM, and there is no basis to invoke its presence in substantial amounts anywhere on Mercury. This conclusion holds even if the variety of ilmenite present is a low-Fe, high-Ti variety more compatible with a highly reduced mineral assemblage (Riner et al., 2010).

In contrast to ilmenite, graphite remains a possible darkening phase on the basis of the GRS elemental abundance limit over the northern hemisphere (Fig. 8). For a ratio of grain sizes of HRP material to darkening material of ⩾20, <1 wt% graphite is required to produce the average northern hemisphere spectrum, and ~5 wt% graphite can yield sufficient darkening to produce LRM. The amount required for LRM is above the limit of the average C abundance over the northern hemisphere, but LRM covers <10% of the northern hemisphere. There are no constraints on C abundance at smaller spatial scales, such as that of Rachmaninoff ejecta. Thus, among coarse-grained phases, only graphite is clearly capable of darkening HRP to LRM. On most inner Solar System bodies, carbon is not an optically dominant phase. However, it is optically dominant in some meteorite analogs to low-albedo asteroids. Although the majority of primitive meteorites have <1 wt% C, some carbonaceous chondrites have ~2–4 wt% C (Jarosewich, 1990; Brown et al., 2000).

Other materials not considered here could alternatively produce the observed darkening of HRP to LRM. One possibility is that thermal processing of sulfide phases, or other aspects of Mercury's surface environment (e.g., prolonged exposure to ultraviolet radiation or the sustained impact of energetic electrons and ions), makes them far darker over geologic time than has been demonstrated over the short time scales of the experiments performed by Helbert et al. (2013). Another is that the darkening component is a phase not considered here, such as a carbide.

4.7. Plausible origins of the darkening phases in LRM

The above results support the hypothesis that LRM is darkened by a component intrinsic to Mercury, which exists within a distinct layer beneath volcanic smooth and intercrater plains units. Such an interpretation agrees with a modeling study of the excavation of subsurface material by large impacts (Rivera-Valentin and Barr, 2014), which predicted that the observed extent of LRM would have been excavated by the late heavy bombardment if it originated from a distinct lower crust ~30 km beneath the surface.

Given that the darkening agent is carbon, possibly in the form of graphite, iron as a mixture of microphase and nanophase grains, or a combination of the two, we offer three working hypotheses for the origin of LRM that are consistent with the above results. First, LRM originates as a deep crustal layer enriched in carbon during planetary differentiation. Three fundamental constraints on Mercury's accretional processes are the large fraction of the planet's mass occupied by its iron-rich core, the low fraction of iron in Mercury's silicates, and the high surface abundance of sulfur. Ebel and Alexander (2011) reviewed pre-MESSENGER models for Mercury's formation. Only one model predicts each of these outcomes. In that model, solar nebula solids at the orbit of Mercury were carbon-rich and similar to anhydrous, chondritic, porous interplanetary dust particles. Condensation of a vapor with this composition produced solids with higher than chondritic Fe/Si ratios, reduced Fe-poor silicates, and sulfides as a refractory phase. In this scenario, a greater than chondritic fraction of carbon could have been incorporated into Mercury during the planet's formation.

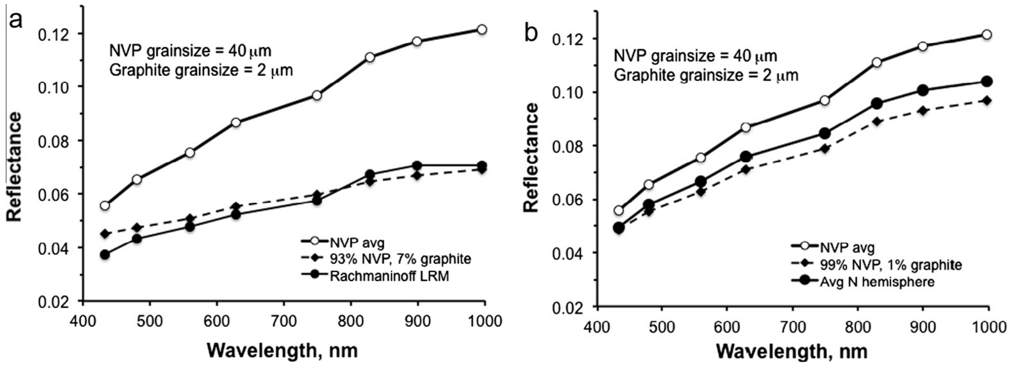

Fig. 8. (a) Example model spectrum of Rachmaninoff LRM for a mixture of 93 wt% NVP with 7 wt% graphite, for 40 μm particles of HRP and 2 μm particles of graphite. (b) Model spectrum of average northern hemisphere materials given the same materials and particle sizes, but with only 1 wt% graphite. Less than 1 wt% graphite can darken HRP to the average spectrum of the northern hemisphere.

Darkening LRM with carbon requires that carbon remain in the crust and not be incorporated into Mercury's core. On the basis of experiments on silicate–metal mixtures at high pressures and temperatures, Dasgupta et al. (2013) found that more C partitions into the metallic core than into the silicate mantle by a factor of ~200–5000. Although that work focused on early Earth, the experimental conditions of 1–5 GPa and 1600–2100 °C have relevance to Mercury, where the core–mantle boundary pressure is estimated to be ~5.5 GPa (Hauck et al., 2013). Even in experiments saturated in graphite, Dasgupta et al. (2013) measured <500 ppm C in the silicate phase and generally <100 ppm. However, core formation on Mercury likely occurred under conditions substantially more reducing than the ~1.5 $\log_{10}$ units below the iron–wüstite buffer (IW-1.5) of the experiments of Dasgupta et al. (2013); estimates of Mercury interior conditions range from IW-4.5 to IW-7.3 (Zolotov et al., 2013; Chabot et al., 2014). Mercury's core has also been suggested to contain additional light elements, such as S and Si (Malavergne et al., 2010; Chabot et al., 2014). The behavior of C in metal–silicate systems at highly reducing conditions and with Si- and S-bearing metals such as those proposed for Mercury is poorly known and outside the range of conditions investigated in experiments to date.

The geochemical modeling of Vander Kaaden and McCubbin (2015) indicates that if C was included in Mercury's mantle, its stable form would have been graphite. Moreover, graphite would have been the only phase likely to be buoyant in an early magma ocean. Vander Kaaden and McCubbin suggested that if Mercury experienced a magma ocean phase, any primary flotation crust must have contained a substantial fraction of C as graphite. Such a crust may be preserved beneath younger flows of plains material, at the several to tens of kilometers depth from which LRM has been excavated. A C-rich flotation crust likely would have been mixed into overlying and underlying materials by impacts and impact melting during the early phases of the late heavy bombardment, producing a relatively thick darkened layer as is inferred for the source region of excavated LRM (Ernst et al., 2015). Darkening of younger volcanic materials by C would require either the presence of C in the magma source region, or incorporation of C from the LRM layer during magma ascent.

Second, LRM could be darkened by the alteration during impact shock of the grain sizes of the low content of preexisting Fe into a mixture of both nanophase and microphase iron or iron sulfide, as suggested by Gillis-Davis et al. (2013). In all or nearly all cases, LRM appears to have been excavated from beneath smooth or intercrater plains (Denevi et al., 2009, 2013a). Conceivably its source region could be a layer that was shocked and melted during or before the part of the late heavy bombardment that preceded plains emplacement. Several percent of a mix of nanophase and microphase Fe can reproduce both the overall reflectance and shape of Mercury's surface spectrum (Riner and Lucey, 2012), abundances consistent with limits from XRS and GRS data. However, mapping of Fe abundance by Weider et al. (2014) shows that Fe content is not strongly correlated with reflectance. Therefore, in this scenario, the physical state and grain size of Fe rather than its abundance would vary, and LRM would be compositionally indistinct.

Third, LRM could be darkened by a C- and Fe-containing veneer that accreted after mantle differentiation, before emplacement of overlying plains. The experimental results of Dasgupta et al. (2013) predict lower C in Earth's silicate reservoirs than is actually measured. Because estimates for the silicate Earth's C content range from ~10 to 500 ppm (Dasgupta and Hirschmann, 2010), Dasgupta et al. concluded that the majority of the C in Earth's mantle postdates the planet's last giant impact. Accretion of a volatile-rich, chondritic, late-stage veneer has been proposed for both Earth and Mars (Wänke, 1981; Wänke and Dreibus, 1994). Once in Mercury's mantle, the stable form of carbon would be graphite. Absent partitioning of elements in the veneer, the expected much greater abundance of iron than carbon in the veneer (Peplowski et al., 2015) would require that iron, occurring in a shocked mix of grain sizes as in the previous case, be responsible for much or most of the darkening.

These three hypotheses make distinct predictions for elemental abundances of carbon and iron in LRM. In the first scenario, C is strongly enriched. In the second scenario, there are no large differences in major element abundances. In the third case, C and especially Fe are present at higher abundances.

4.8. Relationship of color and elemental abundance variations

An aspect of Mercury's color variations that seems surprising, initially, is that the correlation of color with major element abundances is weak and only local. For example, the two large northern hemisphere deposits of HRP, the NVP and Caloris interior plains, are lower in Fe, Mg, Ca, and S and higher in Al than nearby terrain (Weider et al., 2012, 2014, 2015; Nittler et al., 2013). However, globally none of these elements exhibits obvious correlations with reflectance. Areas with high Al other than the two large HRP deposits are low in reflectance (Nittler et al., 2013). And even though large areas of HRP are low in Mg, a large area of ICP is highly enriched in Mg but remains undistinguished by its reflectance and color (Weider et al., 2015). The correlation of Fe with reflectance is weak to non-existent (Weider et al., 2014), so that the abundance of Fe appears not to control reflectance. However, the latter does not rule out a change in the physical state of Fe, from macroscopic grains to dispersed microphase grains as in shock-darkened ordinary chondrites, as a factor in controlling reflectance.

Further consideration suggests that a strong correlation of color and elemental abundance variations on Mercury should not be expected. Recall from Section 1 that the three major factors in determining reflectance and color are the types and abundances of silicates containing large amounts of Fe^{2+}, the presence and abundance of opaque minerals, and the extent of space weathering. The Moon has a surface composition dominated by two very different lithologies, high-reflectance, high-Al, low-Fe anorthosite, and low-reflectance, high-Fe basalt. Reflectance is strongly correlated with Fe and Al abundances, once corrections are made for the effects of space weathering (Lucey et al., 1995, 1998; Blewett et al., 1997). However, those strong correlations among color, reflectance, and elemental abundance are unique so far among airless silicate bodies. 433 Eros is interpreted from its elemental composition to be an undifferentiated ordinary chondrite (Nittler et al., 2001; Lim and Nittler, 2009). On the basis of mapping of near-infrared absorptions contributed by the dominant olivine and pyroxene phases, there appears not to be significant spatial variation in mineralogic composition (Bell et al., 2002; Izenberg et al., 2003), so reflectance and color variations arise entirely from differences in space weathering (Clark et al., 2001; Murchie et al., 2002). Unlike Eros, 4 Vesta is highly differentiated (Russell et al., 2012), with an Fe^{2+}-rich basaltic surface that exhibits pyroxene compositional variations; however, the Fe^{2+} content of silicates is high everywhere, so variations in reflectance and color at 0.4–1.0 μm are dominated instead by a minor darkening component interpreted as exogenic carbonaceous material intermixed with the regolith, and the only measured element correlated (inversely) with reflectance is H (Prettyman et al., 2012).

Mercury's lack of correlation between color and elemental abundance thus appears to result from the absence of a key factor controlling color and reflectance, Fe^{2+} in crustal silicates that is both abundant and exhibits large spatial variations. Olivine, pyroxene, and feldspar, which on the Moon differ strongly in color and reflectance, are all light-toned and spectrally featureless on

Mercury. The dominant spectral trend, between HRP and LRM, is instead interpreted to be the result of spatial variations in the content of a relatively minor opaque phase (the second factor controlling color and reflectance), as on Vesta. Mercury's secondary spectral trend, brightening and a less red spectral slope in fresh crater and bright hollows materials, results from spatial differences in the third factor controlling color and reflectance, space weathering.

5. Conclusions

Acquisition of the MDIS/WAC global, visible-to-near-infrared, eight-color map of Mercury was motivated by the scientific objectives of constraining the formation of geologic units from resolvable differences in color, and constraining mineral composition and compositional heterogeneity of the surface. Multispectral mapping has previously provided key evidence that Mercury's smooth plains have a volcanic origin (Murchie et al., 2008; Head et al., 2008; Denevi et al., 2009) and that the upper crust is vertically heterogeneous, evidence in support of a volcanic origin (Ernst et al., 2010; Denevi et al., 2013a,b). Here we have shown that the color properties of the two largest expanses of smooth plains, the NVP and Caloris interior plains, are distinct from those of remaining smooth plains. Along with this difference in color properties of the NVP and Caloris interior is morphologic evidence for the emplacement of these large expanses of plains by flood volcanism (Head et al., 2011; Ernst et al., 2015). In contrast, the color properties of the remaining population of smooth plains (Denevi et al., 2013a) are closely similar to those of intercrater plains (Whitten et al., 2014), consistent with age being the principal difference between these two types of plains units.

The major spectral trend in the eight-color map results from the difference in reflectance and spectral slope between higher-reflectance, redder volcanic plains and pyroclastic materials (HRP and the red unit) versus darker, less-red LRM. Space weathering forms a secondary trend in which fresher materials are brighter and less red. No units beyond those already described by Robinson et al. (2008) and Denevi et al. (2009) have been resolved at spatial scales sampled by the global map. Measurement and mapping of candidate absorption band depths with eight-color MDIS imaging data do not reveal absorptions associated with sulfide minerals or Fe^{2+}-bearing olivine or pyroxene at the 2% level and a 20-km horizontal scale. This finding is consistent with previous results from MASCS VIRS and the reduced, low-iron silicate composition inferred from those data (Izenberg et al., 2014).

Color properties of LRM provide evidence for its stratigraphic relation with other units and provide insight into its composition. Exposures with nearly the same reflectance and color properties occur in ejecta of craters and basins formed during all periods of Mercury's history. This result is consistent with exposure of intrinsically dark material from depth, rather than formation by gradual space weathering at the surface or the addition of material from the infall of bolides. However, space-weathering effects are superimposed on LRM and may include weakening with exposure age of a broad, shallow 600-nm absorption-like feature. The identity of the darkening phase in LRM is uncertain. Ti-bearing phases can be excluded. Three hypotheses consistent with color and elemental abundance data are that LRM incorporates a primary, graphite-bearing flotation crust formed from an early silicate magma ocean (Vander Kaaden and McCubbin, 2015); that LRM is darkened as a result of alteration of grain sizes of iron by impact shock before and during the late heavy bombardment (Gillis-Davis et al., 2013); and that LRM is darkened by a late-accreting iron- and carbon-bearing veneer. In either case, the LRM was buried by younger intercrater and smooth plains and subsequently excavated. Other possibilities for the darkening phase in LRM include sulfides, if they can be darkened by heating or thermal cycling to greater degrees than have been demonstrated in the laboratory, or an exotic mineral not yet considered. Decoupling of color and elemental abundance variations probably results from crustal silicates having very low contents of Fe^{2+}, such that reflectance is controlled instead by minor opaque phases and the extent of space weathering.

Several areas of needed future analysis and modeling are called out by the results described in this paper: (a) Although tens-of-kilometers-scale deposits of sulfide minerals are not resolved in the global map, smaller deposits may exist and be detectable in higher-resolution MDIS/WAC data. We note in particular evidence described by Vilas et al. (2014) for kilometer-scale deposits of sulfide minerals in association with some hollows. (b) The lower values of PC2 and the less red spectral slope associated with Mercury's hot poles are reproducible in both MDIS/WAC and MASCS/VIRS data. An important investigation will be whether this pattern can be shown to result from the maturation of nanophase metallic iron formed by space weathering into coarser grains that impart a grayer color to the surface, e.g., by Ostwald ripening (Noble and Pieters, 2003). (c) Comprehensive studies of LRM, including high-resolution 11-color measurements acquired during MESSENGER's extended mission, will provide new constraints on the stratigraphy of LRM and can be used to test whether the observed spectral heterogeneity of LRM results from space weathering of a single composition or from the presence of two indigenous darkening components. (d) The current analysis of GRS data falls short of a detection of carbon, but further reduction in uncertainties or low-altitude measurements by MESSENGER's Neutron Spectrometer might improve constraints on C abundance (Peplowski et al., 2015). (e) Improved understanding of C partitioning during Mercury's formation and evolution would also be important. Specific topics for future investigation should include the form that C would take in magmas, its solubility in silicate melts under highly reducing conditions, its partitioning between the mantle and a core with a large S or Si content, and the potential occurrence of exotic minerals such as carbides.

Acknowledgments

The MESSENGER mission is supported by the NASA Discovery Program under contracts NAS5-97271 to The Johns Hopkins University Applied Physics Laboratory and NASW-00002 to the Carnegie Institution of Washington. Several authors acknowledge support from the MESSENGER Participating Scientist program. We are grateful for constructive discussions with David Lawrence, Francis McCubbin, Patrick Peplowski, and Kathleen Vander Kaaden.

References

Adams, J.B., McCord, T.B., 1970. Remote sensing of lunar surface mineralogy: Implications from visible and near-infrared reflectivity of Apollo 11 samples. Proc. Apollo 11 Lunar Sci. Conf. 3, 1937–1945.

Bell, J.F. et al., 2002. Near-IR reflectance spectroscopy of 433 Eros from the NIS instrument on the NEAR mission. I. Low phase angle observations. Icarus 155, 119–144.

Blewett, D.T. et al., 1997. Clementine images of the lunar sample-return stations: Refinement of FeO and TiO_2 mapping techniques. J. Geophys. Res. 102, 16319–16325.

Blewett, D.T. et al., 2009. Multispectral images of Mercury from the first MESSENGER flyby: Analysis of global and regional color trends. Earth Planet. Sci. Lett. 285, 272–282. http://dx.doi.org/10.1016/j.epsl.2009.02.021.

Blewett, D.T. et al., 2011. Hollows on Mercury: Evidence from MESSENGER for geologically recent volatile-related activity. Science 333, 1856–1859.

Blewett, D.T. et al., 2013. Mercury's hollows: Constraints on formation and composition from analysis of geological setting and spectral reflectance. J. Geophys. Res. Planets 118, 1013–1032. http://dx.doi.org/10.1029/2012JE004174.

Braden, S.E., Robinson, M.S., 2013. Relative rates of optical maturation of regolith on Mercury and the Moon. J. Geophys. Res. Planets 118, 1903–1914. http://dx.doi.org/10.002/jgre20143.

Britt, D.T., Pieters, C.M., 1994. Darkening in black and gas-rich ordinary chondrites: The spectral effects of opaque morphology and distribution. Geochim. Cosmochim. Acta 58, 3905–3919.

Brown, P.E. et al., 2000. The fall, recovery, orbit, and composition of the Tagish Lake meteorite: A new type of carbonaceous chondrite. Science 290, 320–325.

Brownlee, D., Joswiak, D., Matrajt, G., 2012. Overview of the rocky component of Wild 2 comet samples: Insight into the early Solar System, relationship with meteoritic materials and the differences between comets and asteroids. Meteorit. Planet. Sci. 47, 453–470.

Bruck Syal, M., Schultz, P.H., Riner, M.A., 2015. Darkening of Mercury's surface by cometary carbon. Nature Geosci. http://dx.doi.org/10.1038/ngeo2397, in press.

Burbine, T.H. et al., 2002. Spectra of extremely reduced assemblages: Implications for Mercury. Meteorit. Planet. Sci. 37, 1233–1244.

Bus, S.J., Binzel, R.P., 2002. Phase II of the Small Main-Belt Asteroid Spectroscopic Survey: A feature-based taxonomy. Icarus 158, 146–177.

Byrne, P.K. et al., 2013. An assemblage of lava flow features on Mercury. J. Geophys. Res. Planets 118, 1303–1322. http://dx.doi.org/10.1002/jgre.20052.

Chabot, N.L. et al., 2014. Experimental constraints on Mercury's core formation. Earth Planet. Sci. Lett. 390, 199–208. http://dx.doi.org/10.1016/j.epsl.2014.01.004.

Charette, M.P., McCord, T.B., Pieters, J.B., 1974. Application of remote spectral reflectance measurements to lunar geology classification and determination of titanium content of lunar soils. J. Geophys. Res. 79, 1605–1613.

Clark, B. et al., 2001. Space weathering on Eros: Constraints from albedo and spectral measurements of Psyche Crater. Meteorit. Planet. Sci. 36, 1617–1637.

Clark, R.N., Roush, T.L., 1984. Reflectance spectroscopy: Quantitative analysis techniques for remote sensing applications. J. Geophys. Res. 89, 6329–6340.

Clark, R.N. et al., 2012. The surface composition of Iapetus: Mapping results from Cassini VIMS. Icarus 218, 831–860. http://dx.doi.org/10.1016/j.icarus.2012.01.008.

Cloutis, E.A. et al., 2011. Spectral reflectance properties of carbonaceous chondrites: 2. CM chondrites. Icarus 216, 309–346. http://dx.doi.org/10.1016/j.icarus.2011.09.009.

Dasgupta, R., Hirschmann, M.M., 2010. The deep carbon cycle and melting in Earth's interior. Earth Planet. Sci. Lett. 298, 1–13.

Dasgupta, R. et al., 2013. Carbon solution and partitioning between metallic and silicate melts in a shallow magma ocean: Implications for the origin and distribution of terrestrial carbon. Geochim. Cosmochim. Acta 102, 191–212.

Denevi, B.W., Robinson, M.S., 2008. Mercury's albedo from Mariner 10: Implications for the presence of ferrous iron. Icarus 197, 239–246. http://dx.doi.org/10.1016/j.icarus.2008.04.021.

Denevi, B.W. et al., 2009. The evolution of Mercury's crust: A global perspective from MESSENGER. Science 324, 613–618. http://dx.doi.org/10.1126/science.1172226.

Denevi, B.W. et al., 2013a. The distribution and origin of smooth plains on Mercury. J. Geophys. Res. Planets 118, 891–907. http://dx.doi.org/10.1002/jgre.20075.

Denevi, B.W. et al., 2013b. The volcanic origin of a region of intercrater plains on Mercury. Lunar Planet. Sci. 44. Abstract 1218.

De Sanctis, M.C. et al., 2012. Spectroscopic characterization of mineralogy and its diversity across Vesta. Science 336, 697–700.

Domingue, D.L. et al., 2014. Mercury's weather-beaten surface: Understanding Mercury in the context of lunar and asteroidal space weathering studies. Space Sci. Rev. 181, 121–214.

Domingue, D.L. et al., 2015. Mercury's global color mosaic: An update from MESSENGER's orbital observations. Icarus, in press. http://dx.doi.org/10.1016/j.icarus.2014.11.027.

Dzurisin, D., 1978. The tectonic and volcanic history of Mercury as inferred from studies of scarps, ridges, troughs, and other lineaments. J. Geophys. Res. 83, 4883–4906.

Ebel, D.S., Alexander, C.M.O'D., 2011. Equilibrium condensation from chondritic porous IDP enriched vapor: Implications for Mercury and enstatite chondrite origins. Planet. Space Sci. 59, 1888–1894.

Ernst, C.M. et al., 2010. Exposure of spectrally distinct material by impact craters on Mercury: Implications for global stratigraphy. Icarus 209, 210–223.

Ernst, C.M. et al., 2015. Stratigraphy of the Caloris basin, Mercury: Implications for volcanic history and basin impact melt. Icarus 250, 413–429.

Evans, R.G. et al., 2012. Major-element abundances on the surface of Mercury: Results from the MESSENGER Gamma-Ray Spectrometer. J. Geophys. Res. 117, E00L07. http://dx.doi.org/10.1029/2012JE004178.

Fassett, C.I. et al., 2009. Caloris impact basin: Exterior geomorphology, stratigraphy, morphometry, radial sculpture, and smooth plains deposits. Earth Planet. Sci. Lett. 285, 297–308. http://dx.doi.org/10.1016/j.epsl.2009.05.022.

Fassett, C.I. et al., 2012. Large impact basins on Mercury: Global distribution, characteristics, and modification history from MESSENGER orbital data. J. Geophys. Res. 117, E00L08. http://dx.doi.org/10.1029/2012JE004154.

Gaffey, S.J. et al., 1993. Ultraviolet, visible, and near-infrared reflectance spectroscopy: Laboratory spectra of geologic materials. In: Pieters, C.M., Englert, P.A.J. (Eds.), Remote Geochemical Analysis: Elemental and Mineralogic Composition. Cambridge University Press, Cambridge, U.K., pp. 43–78.

Gillis-Davis, J.J. et al., 2013. Impact darkening: A possible mechanism to explain why Mercury is spectrally dark and featureless. Abstract P11A-07 Presented at 2013 Fall Meeting, AGU, San Francisco, California, 9–13 December.

Goudge, T.A. et al., 2014. Global inventory and characterization of pyroclastic deposits on Mercury: New insights into pyroclastic activity from MESSENGER orbital data. J. Geophys. Res.: Planets 119, 635–658. http://dx.doi.org/10.1002/2013JE0004480.

Hapke, B., 2001. Space weathering from Mercury to the asteroid belt. J. Geophys. Res. 106, 10039–10073.

Hapke, B., 2012. Theory of Reflectance and Emittance Spectroscopy. Cambridge University Press, New York.

Hauck II, S.A. et al., 2013. The curious case of Mercury's internal structure. J. Geophys. Res. Planets 118, 1204–1220. http://dx.doi.org/10.1002/jgre.20091.

Hawkins III, S.E. et al., 2007. The Mercury Dual Imaging System on the MESSENGER spacecraft. Space Sci. Rev. 131, 247–338.

Hawkins III, S.E. et al., 2009. In-flight performance of MESSENGER's Mercury Dual Imaging System. In: Hoover, R.B., Levin, G.V., Rozanov, A.Y., Retherford, K.D. (Eds.), Instruments and Methods for Astrobiology and Planetary Missions XII, SPIE Proceedings, vol. 7441. SPIE, Bellingham, Wash. Paper 74410Z, 12pp.

Head, J.W. et al., 2008. Volcanism on Mercury: Evidence from the first MESSENGER flyby. Science 321, 69–72.

Head, J.W. et al., 2009a. Volcanism on Mercury: Evidence from the first MESSENGER flyby for extrusive and explosive activity and the volcanic origin of plains. Earth Planet. Sci. Lett. 285, 227–242. http://dx.doi.org/10.1016/j.epsl.2009.03.007.

Head, J.W. et al., 2009b. Evidence for intrusive activity on Mercury from the first MESSENGER flyby. Earth Planet. Sci. Lett. 285, 251–262. http://dx.doi.org/10.1016/j.epsl.2009.03.008.

Head, J.W. et al., 2011. Flood volcanism in the high northern latitudes of Mercury revealed by MESSENGER. Science 333, 1853–1856.

Heiken, G.H., Vaniman, D.T., 1990. Characterization of lunar ilmenite resources. Proc. Lunar. Sci. Conf. 20, 239–247.

Helbert, J., Maturilli, A., D'Amore, M., 2013. Visible and near-infrared reflectance spectra of thermally processed synthetic sulfides as a potential analog for the hollow forming materials on Mercury. Earth Planet. Sci. Lett. 369, 233–238.

Hurwitz, D.M. et al., 2013. Investigating the origin of candidate lava channels on Mercury with MESSENGER data: Theory and observations. J. Geophys. Res.: Planets 118, 471–486. http://dx.doi.org/10.1029/2012JE004103.

Iacono-Marziano, G. et al., 2012. Extremely reducing conditions reached during basaltic intrusion in organic matter-bearing sediments. Earth Planet. Sci. Lett. 357, 319–326.

Izenberg, N.R. et al., 2003. Spectral properties and geologic processes on Eros from combined NEAR NIS and MSI data sets. Meteorit. Planet. Sci. 38, 1053–1077.

Izenberg, N.R. et al., 2014. The low-iron, reduced surface of Mercury as seen in spectral reflectance by MESSENGER. Icarus 228, 364–374. http://dx.doi.org/10.1016/j.icarus.2013.10.023.

Jarosewich, E., 1990. Chemical analyses of meteorites: A compilation of stony and iron meteorite analyses. Meteoritics 25, 323–337.

Keller, M.R. et al., 2013. Time-dependent calibration of MESSENGER's wide-angle camera following a contamination event. Lunar Planet. Sci. 44. Abstract 1719.

Kerber, L. et al., 2009. Explosive volcanic eruptions on Mercury: Eruption conditions, magma volatile content, and implications for interior volatile abundances. Earth Planet. Sci. Lett. 285, 263–271. http://dx.doi.org/10.1016/j.epsl.2009.04.037.

Kerber, L. et al., 2011. The global distribution of pyroclastic deposits on Mercury: The view from MESSENGER flybys 1–3. Planet. Space Sci. 59, 1895–1909. http://dx.doi.org/10.1016/j.pss.2011.03.020.

Klima, R.L., Dyar, M.D., Pieters, C.M., 2011. Near-infrared spectra of clinopyroxenes: Effects of calcium content and crystal structure. Meteorit. Planet. Sci. 42, 235–253.

Klimczak, C. et al., 2012. Deformation associated with ghost craters and basins in volcanic smooth plains on Mercury: Strain analysis and implications for plains evolution. J. Geophys. Res. 117, E00L03. http://dx.doi.org/10.1029/2012JE004100.

Kurucz, R.L., 1997. The SOLAR Irradiance by Computation. <http://kurucz.harvard.edu/sun/irradiance/>.

Lim, L.F., Nittler, L.R., 2009. Elemental composition of 433 Eros: New calibration of the NEAR-Shoemaker XRS data. Icarus 200, 129–146.

Lodders, K., Fegley, B., 1992. Lanthanide and actinide condensation into oldhamite under reducing conditions. Lunar Planet. Sci. 23. Abstract 797.

Lucey, P.G., Riner, M.A., 2011. The optical effects of small iron particles that darken but do not redden: Evidence of intense space weathering on Mercury. Icarus 212, 451–462. http://dx.doi.org/10.1016/j.icarus.2011.01.022.

Lucey, P.G., Taylor, G.J., Malaret, E., 1995. Abundance and distribution of iron on the Moon. Science 268, 1150–1153.

Lucey, P.G., Blewett, D.T., Hawke, B.R., 1998. Mapping the FeO and TiO_2 content of the lunar surface with multispectral imaging. J. Geophys. Res. 103, 3679–3699.

Ma, C., Beckett, J.R., Rossman, G.R., 2012. Discovery of buseckite, (Fe,Zn,Mn)S, a new mineral in Zakłodzie, an ungrouped enstatite-rich achondrite. Lunar Planet. Sci. 43. Abstract 1520.

Malavergne, V. et al., 2010. Highly reducing conditions during core formation on Mercury: Implications for internal structure and the origin of a magnetic field. Icarus 206, 199–209.

Malin, M.C., 1976. Observations of intercrater plains on Mercury. Geophys. Res. Lett. 3, 581–584.

McClintock, W.E., Lankton, M.R., 2007. The Mercury Atmospheric and Surface Composition Spectrometer for the MESSENGER mission. Space Sci. Rev. 131, 481–522.

McClintock, W.E. et al., 2008. Spectroscopic observations of Mercury's surface reflectance during MESSENGER's first Mercury flyby. Science 321, 62–65.

McCord, T.B., Clark, R.N., 1979. The Mercury soil: Presence of Fe^{2+}. J. Geophys. Res. 84, 7664–7668.
McCord, T.B. et al., 2012. Dark material on Vesta: Characteristics, sources and implications. Nature 491, 83–86.
McCoy, T.J., Dickinson, T.L., Lofgren, G.E., 1999. Partial melting of the Indarch (EH4) Meteorite: A textural, chemical and phase relations view of melting and melt migration. Meteorit. Planet. Sci. 34, 735–746.
McCubbin, F.M. et al., 2012. Is Mercury a volatile-rich planet? Geophys. Res. Lett. 39, L09202. http://dx.doi.org/10.1029/2012GL051711.
McKay, D.S. et al., 1991. The lunar regolith. In: Heiken, G., Vaniman, D., French, B.M. (Eds.), Lunar Sourcebook. Cambridge University Press, Cambridge, U.K., pp. 285–356.
Morris, R.V. et al., 1985. Spectral and other physicochemical properties of submicron powders of hematite (α-Fe_2O_3), maghemite (γ-Fe_2O_3), magnetite (Fe_3O_4), goethite (α-FeOOH), and lepidocrocite (γ-FeOOH). J. Geophys. Res. 90, 3126–3144.
Murchie, S.L., 2013. MESSENGER MDIS Calibrated Data Catalog. <http://pds-imaging.jpl.nasa.gov/data/messenger/msgrmds_2001/CATALOG/MDIS_CDR_DS.CAT>.
Murchie, S.L. et al., 2002. Color properties of Eros from NEAR multispectral imaging. Icarus 155, 145–168.
Murchie, S.L. et al., 2008. Geology of the Caloris basin, Mercury: A view from MESSENGER. Science 321, 73–77.
Mustard, J.F., Pieters, C.M., 1989. Photometric phase functions of common geologic minerals and applications to quantitative analysis of mineral mixture reflectance spectra. J. Geophys. Res. 94, 13619–13634.
Nittler, L.R. et al., 2001. X-ray fluorescence measurements of the surface elemental composition of Asteroid 433 Eros. Meteorit. Planet. Sci. 36, 1673–1695.
Nittler, L.R. et al., 2011. The major-element composition of Mercury's surface from MESSENGER X-Ray Spectrometry. Science 333, 1847–1850.
Nittler, L.R. et al., 2013. Mapping major element abundances on Mercury's surface with MESSENGER X-Ray Spectrometer data. Lunar Planet. Sci. 44. Abstract 2458.
Noble, S.K., Pieters, C.M., 2003. Space weathering on Mercury: Implications for remote sensing. Solar Syst. Res. 37, 31–35.
Noguchi, T. et al., 2011. Incipient space weathering observed on the surface of Itokawa dust particles. Science 333, 1121–1125.
Noguchi, T. et al., 2014. Space weathered rims found on the surfaces of the Itokawa dust particles. Meteorit. Planet. Sci. 49, 188–214. http://dx.doi.org/10.1111/maps.12111.
Oberbeck, V.R. et al., 1977. Comparative studies of lunar, martian, and mercurian craters and plains. J. Geophys. Res. 82, 1681–1698.
Peplowski, P.N. et al., 2015. Constraints on the abundance of carbon in near-surface materials on Mercury: Results from the MESSENGER Gamma-Ray Spectrometer. Planet. Space Sci. 108, 99–107. http://dx.doi.org/10.1016/j.pss.2015.01.008.
Pieters, C.M., 1993. Compositional diversity and stratigraphy of the lunar crust derived from reflectance spectroscopy. In: Pieters, C.M., Englert, P.A.J. (Eds.), Remote Geochemical Analysis: Elemental and Mineralogic Composition. Cambridge University Press, Cambridge, U.K., pp. 309–340.
Pieters, C.M. et al., 2012. Distinctive space weathering on Vesta from regolith mixing processes. Nature 491, 79–82. http://dx.doi.org/10.1038/nature11534.
Prettyman, T.H. et al., 2012. Elemental mapping by Dawn reveals exogenic H in Vesta's regolith. Science 338, 242–246.
Prockter, L.M. et al., 2010. Evidence for young volcanism on Mercury from the third MESSENGER flyby. Science 329, 668–671. http://dx.doi.org/10.1126/science.1188186.
Reddy, V. et al., 2012a. Color and albedo heterogeneity of Vesta from Dawn. Science 336, 700–704.
Reddy, V. et al., 2012b. Delivery of dark material to Vesta via carbonaceous chondritic impacts. Icarus 221, 544–559.
Riner, M.A., Lucey, P.G., 2012. Spectral effects of space weathering on Mercury: The role of composition and environment. Geophys. Res. Lett. 39, L12201. http://dx.doi.org/10.1029/2012GL052065.
Riner, M.A. et al., 2009. Nature of opaque components on Mercury: Insights into a mercurian magma ocean. Geophys. Res. Lett. 36, L02201. http://dx.doi.org/10.1029/2008GL036128.
Riner, M.A. et al., 2010. Mercury surface composition: Integrating petrologic modeling and remote sensing data to place constraints on FeO abundance. Icarus 209, 301–313.
Rivera-Valentin, E.G., Barr, A.C., 2014. Impact-induced compositional variations on Mercury. Earth Planet. Sci. Lett. 391, 234–242. http://dx.doi.org/10.1016/j.epsl.2014.02.003.
Robinson, M.S., Lucey, P.G., 1997. Recalibrated Mariner 10 color mosaics: Implications for mercurian volcanism. Science 275, 197–200.
Robinson, M.S. et al., 2008. Reflectance and color variations on Mercury: Regolith processes and compositional heterogeneity. Science 321, 66–69.
Rubin, A.E., 1997. Igneous graphite in enstatite chondrites. Mineral. Mag. 61, 699–703.
Russell, C.T. et al., 2012. Dawn at Vesta: Testing the protoplanetary paradigm. Science 336, 684–686. http://dx.doi.org/10.1126/science.1219381.
Solomon, S.C. et al., 2001. The MESSENGER mission to Mercury: Scientific objectives and implementation. Planet. Space Sci. 49, 1445–1465.
Sprague, A.L., Hunten, D.M., Lodders, K., 1995. Sulfur at Mercury, elemental at the poles and sulfides in the regolith. Icarus 118, 211–215. http://dx.doi.org/10.1006/icar.1995.1186.
Spudis, P.D., Guest, J.E., 1988. Stratigraphy and geologic history of Mercury. In: Vilas, F., Chapman, C.R., Matthews, M.S. (Eds.), Mercury. University of Arizona Press, Tucson, AZ, pp. 118–164.
Strom, R.G., Neukum, G., 1988. The cratering record on Mercury and the origin of impacting objects. In: Vilas, F., Chapman, C.R., Matthews, M.S. (Eds.), Mercury. University of Arizona Press, Tucson, AZ, pp. 336–373.
Strom, R.G., Trask, N.J., Guest, J.E., 1975. Tectonism and volcanism on Mercury. J. Geophys. Res. 80, 2478–2507.
Trask, N.J., Guest, J.E., 1975. Preliminary geologic terrain map of Mercury. J. Geophys. Res. 80, 2461–2477.
Ulff-Moller, F., 1990. Formation of native iron in sediment-contaminated magma: I. A case study of the Hanekammen Complex on Disko Island, West Greenland. Geochim. Cosmochim. Acta 54, 57–70.
Vander Kaaden, K.E., McCubbin, F.M., 2015. Exotic crust formation on Mercury: Consequences of a shallow, FeO-poor mantle. J. Geophys. Res.: Planets 120, 195–209. http://dx.doi.org/10.1002/2014JE004733.
Vilas, F., 1988. Surface composition of Mercury from reflectance spectrophotometry. In: Vilas, F., Chapman, C.R., Matthews, M.S. (Eds.), Mercury. University of Arizona Press, Tucson, AZ, pp. 59–76.
Vilas, F. et al., 2014. Dominici crater wall hollows: Potential spectral evidence for sulfide mineralogy on Mercury. Lunar Planet. Sci. 45. Abstract 1296.
Wänke, H., 1981. Constitution of terrestrial planets. Philos. Trans. R. Soc. Lond. A 303, 287–302.
Wänke, H., Dreibus, G., 1994. Water abundance and accretion history of terrestrial planets. Papers Presented to the Conference on Deep Earth and Planetary Volatiles. Lunar and Planetary Institute, Houston, TX, p. 46.
Warell, J., 2004. Properties of the hermean regolith: 4. Photometric parameters of Mercury and the Moon contrasted with Hapke modeling. Icarus 167, 271–286.
Warell, J., Blewett, D.T., 2004. Properties of the hermean regolith: V. New optical reflectance spectra, comparison with lunar anorthosites, and mineralogical modeling. Icarus 168, 257–276.
Weider, S.Z. et al., 2012. Chemical heterogeneity on Mercury's surface revealed by the MESSENGER X-Ray Spectrometer. J. Geophys. Res. 117, E00L05. http://dx.doi.org/10.1029/2012JE004153.
Weider, S.Z. et al., 2014. Variations in the abundance of iron on Mercury's surface from MESSENGER X-Ray Spectrometer observations. Icarus 235, 170–186. http://dx.doi.org/10.1016/j.icarus.2014.03.002.
Weider, S.Z. et al., 2015. Evidence for geochemical terranes on Mercury: Global mapping of major elements with MESSENGER's X-Ray Spectrometer. Earth Planet. Sci. Lett. 416, 109–120.
Whitten, J.L. et al., 2014. Intercrater plains on Mercury: Insights into unit definition, characterization, and origin from MESSENGER datasets. Icarus 241, 97–113. http://dx.doi.org/10.1016/j.icarus.2014.06.013.
Wilhelms, D.E., 1976. Mercurian volcanism questioned. Icarus 28, 551–558.
Zolotov, M. et al., 2013. The redox state, FeO content, and origin of sulfur-rich magmas on Mercury. J. Geophys. Res.: Planets 118, 138–146.